

A precessing jet from a supermassive black hole: multi-wavelength observations of S5 1044+71

M. Cerruti^{a,*}, P. A. Duverne^{a,*}, G. Ganesaratnam^{b,*}, P. Goswami^{c,a,*}, H. X. Ren^{d,*} and N. Sahakyan^{e,*}

^aUniversité Paris Cité, CNRS, Astroparticule et Cosmologie, Paris, F-75013, France

^aInstitut d'Astrophysique Spatiale, Orsay, F-91405, France

^cZAH Landessternwarte, Universität Heidelberg, Königstuhl 12, Heidelberg, D-69029, Germany

^dMax-Planck-Institut für Kernphysik, PO Box 103980, Heidelberg, D-69029, Germany

^eICRANet-Armenia, Marshall Baghramian Avenue 24a, Yerevan, AM-0019, Armenia

ARTICLE INFO

Keywords:

Gamma rays: galaxies

Radiation mechanisms: non-thermal

quasars:individual:S51044-71

ABSTRACT

The bright γ -ray blazar S5 1044+71 has been identified as showing very significant quasi-periodic oscillations in the *Fermi*-LAT data in recent studies, with a periodicity of about three years. With the completion of a new three-year γ -ray cycle, we aim to revisit the periodicity in *Fermi*-LAT data, and analyze all available multi-wavelength (MWL) data to search for possible correlations and time-lags. These observations will be used to test for the compatibility of the observed periodicity with a precessing jet from the supermassive black hole powering the blazar. We analyze data from *Fermi*-LAT (γ -rays), *NuSTAR*, *Swift*-XRT, and *AstroSat*-SXT (X-rays), *Swift*-UVOT, *AstroSat*-UVIT, ASAS-SN, ZTF, Pan-STARRS (ultraviolet and optical), and NEOWISE (infrared). In addition we present an analysis from historical observations from the Palomar and Pulkovo observations. Single-band spectral variability, MWL correlations, and cross-correlations are computed. We then model the *Fermi*-LAT light curve with a precessing jet model, providing constraints on the geometry of the system and providing the evolution of the Doppler factor with time. The latter is used as input for MWL fitting of the spectral energy distribution to constrain the physical properties of the emitting region in the jet. We confirm previous claims on the existence of a periodic γ -ray signal in S5 1044+71. We detect significant spectral variability in γ -ray, X-rays, and optical/UV data. We detect significant correlation between low-energy (infrared/optical/ultraviolet) data and γ -rays, with a correlation index of about 1; the correlation between X-rays and γ -rays is milder, with a correlation index of about 0.3. We do not detect any significant time-lag between bands. The *Fermi*-LAT light curve is successfully fit by a precessing jet model. The fit to the spectral energy distributions indicate that S5 1044+71 is a typical blazar, in which the γ -ray emission is located beyond the broad-line region. The existence of a periodic γ -ray signal S5 1044+71 is confirmed. All the MWL observations we present in this work are consistent with the existence of a precessing relativistic jet from the supermassive black hole.

1. Introduction

The extragalactic γ -ray sky is dominated by Active Galactic Nuclei (AGNs), accreting supermassive black holes (SMBHs) with masses ranging from 10^6 to $10^8 M_\odot$, located at cosmological distances. The large majority of γ -ray AGNs belong to the class of blazars (Abdollahi et al., 2022), which are characterized by rapid variability, a spectral energy distribution (SED) showing a broad non-thermal continuum from radio to TeV energies, and a high degree of polarization in radio, optical, and X-rays (see e.g. Blandford et al., 2019, for a recent review). High angular resolution radio observations of these objects show a core-dominated morphology with a single jet-like structure (e.g. Lister et al., 2009). These observational characteristics are well explained within the AGN unified model assuming that blazars are radio-loud AGNs (i.e. objects in which the accretion of matter onto the SMBH is accompanied by the launching of two jets of plasma along the polar axis of the black hole) whose jet

is closely aligned to the line of sight (Urry and Padovani, 1995). The small angle to the observer implies a large value of the relativistic Doppler factor δ that takes a value typically $\delta \geq 10$. The emission from the jet is thus Doppler-boosted in the reference frame of the observer, and dominates blazar SEDs. From an observational point of view, blazars are classified into two subclasses, flat-spectrum-radio-quasars (FSRQs) and BL Lacertae objects, according to the presence (in the former) or absence (in the latter) of emission lines in the optical/UV spectrum. In blazar leptonic radiative models, the γ -ray emission is produced via inverse Compton scattering of low-energy photons by electrons/positrons in the jet. In FSRQs, the photons upscattered to γ -rays are external to the jet, and are the emission lines from the broad-line-region (BLR) and the thermal black-body radiation from the dusty torus (for further details see e.g. Cerruti, 2020, for a recent review on radiative modeling in blazars).

The Large Area Telescope (LAT, Atwood et al., 2009) on board the *Fermi* satellite has significantly improved our knowledge of γ -ray blazars, in particular thanks to its survey capabilities designed to monitor the whole sky about every three hours. Uninterrupted γ -ray light curves on thousands of blazars are thus available since the launch of the *Fermi*

*Corresponding author

✉ cerruti@apc.in2p3.fr (M. Cerruti); duverne@apc.in2p3.fr (P.A. Duverne); ganushan.ganesaratnam@ias.u-psud.fr (G. Ganesaratnam);

pgoswami@lsw.uni-heidelberg.de (P. Goswami); helena.ren@mpi-hd.mpg.de (H.X. Ren); narek.sahakyan@icranet.org (N. Sahakyan)

ORCID(s):

satellite in June 2008, and represent a unique dataset to study blazar variability.

One of the unexpected discoveries in LAT AGN observations is the periodicity in the light curves of some of these γ -ray blazars, with periods ranging from months to years. The first hint (3σ) for periodic modulation was seen in PG 1553+113 by Ackermann et al. (2015). Following this first tentative detection, many authors have extensively studied periodic or quasi-periodic oscillations (QPOs) in LAT blazars (see Covino et al., 2020; Peñil et al., 2020; Yang et al., 2021, and references therein). Although many of these results are of low significance and become compatible with noise once the large trial factors are included (Ren et al., 2023; Peñil et al., 2025), some periodicities seem solid: besides PG 1553+113, among the significant QPO detections, it might be worth mentioning the one in PKS 2247-131 (Zhou et al., 2018). The work presented in Ren et al. (2023) investigates QPOs in a sample made of the 35 brightest LAT AGNs, and identifies the source S5 1044+71 (an FSRQ at redshift $z = 1.15$) among the most significant candidates. The object shows a QPO behavior with a period of about 3 years ($P = 1100 \pm 200$ days). The original work shows three full cycles of the periodic signal. The overall significance was lowered by the fact that the first supposed maximum was strongly suppressed compared to the next ones, likely due to the intrinsic blazar variability. The same periodicity in S5 1044+71 is identified by Wang et al. (2022). A multi-wavelength (MWL) data analysis of the object was presented in Kun et al. (2022), covering the same data as in Ren et al. (2023), i.e. four full cycles assuming the first one was suppressed due to blazar variability. VLBI radio observations are shown in Kun et al. (2022), showing that the kpc and pc jets are misaligned by about 90° , suggesting jet precession. A more recent follow-up study in γ -ray and radio by the same authors is presented in Kun et al. (2024), covering part of the fifth maximum (including data up to June 2023).

Several models have been developed to explain γ -ray QPOs in blazars. They can be split in to families: geometric models, in which the periodic modulations are due to changes in the viewing angle of the emitting region, and thus to changes in the Doppler factor δ ; and accretion-ejection coupling models, in which the periodicities are produced at the level of the accretion flow, and propagate into the jet and thus in the γ -ray light curve (as discussed in Valtonen et al., 2009, for an application to OJ 287). Concerning geometric models, two main options arise: either the whole jet change its angle to the observer (see Begelman et al., 1980; Sobacchi et al., 2017), or the γ -ray emitting region is a sub-structure in the jet, and the QPO track its motion in the jet, for example in the form of a helical path giving access to jet structure (Rieger, 2004). In the first case, the fact that the jet is precessing, or that the SMBH itself is moving on a circular object, could imply the existence of a companion massive enough to produce this effect, and hence open the window

to detect and study SMBH binaries in the Universe.

In this work, we present a new MWL analysis of S5 1044+71 that incorporates updated *Fermi*-LAT observations covering five full cycles, together with X-ray data *NuSTAR*, *Swift*-XRT and *AstroSat*-SXT; optical/UV measurements from *Swift*-UVOT and *AstroSat*-UVIT, and additional archival optical and IR data from surveys including ASAS-SN, ZTF, Pan-STARRS1 and NEOWISE. Furthermore, we explored historical optical observations from Palomar and Pulkovo, obtained via the NAROO project (Robert et al., 2021). Following the results by Kun et al. (2022), that suggests that the periodicity is related to jet precession, we focus on this radiative scenario. The present work extends previous studies in three key directions. First, the detection of a new γ -ray maximum at the epoch predicted by Ren et al. (2023) provides an a-posteriori confirmation of the ~ 3 -year timescale of the QPO. Second, we perform a comprehensive MWL variability and correlation analysis over more than a decade of observations, allowing us to compare flux-flux relations and time-lag properties across multiple activity cycles. Finally, we combine the variability analysis with a time-dependent geometrical model and multi-epoch SED modeling, enabling us to constrain the jet precession scenario in a self-consistent framework.

This paper is structured as follows: in section 2 we present the data analysis from all instruments; in section 3.1 we analyze the variability properties of the dataset, including spectral variability within a band, MWL correlations, search for time lags, and revisited QPO search; in section 4 we present a modeling of the LAT light curve; in section 5 we present a MWL modeling of the SED; in section 6 we provide discussion and conclusions.

2. Multi-wavelength observations

2.1. *Fermi*-LAT

The LAT (Atwood et al., 2009) instrument onboard the *Fermi* satellite is a pair-conversion detector, sensitive to photons with energy ranging from 20 MeV to 300 GeV and it carries out an all-sky survey every 3 hours. The γ -ray data used in this work were obtained from the Markarian Multiwavelength Data Center (MMDC). Specifically, we used the adaptively binned γ -ray light curve, and the results of spectral analyses performed over different periods (Sahakyan et al., 2024b). The data reduction is performed using *fermitools* (version 2.0.8) with the P8R3_SOURCE_V3 instrument response functions. Events in the 100 MeV–300 GeV energy range are selected within a 12° region centered on the γ -ray position of S5 1044+71 (RA= 162.11, Dec= 71.73). The dataset we use covers a time period starting from August 4, 2008, to August 4, 2025 (MET 239667417–775958405) and includes only events classified as *evclass*=128 and *evtype*=3. To minimize contamination from Earth-limb photons, events with zenith angles larger than 90° are excluded. Then, we apply a likelihood analysis that includes

A precessing jet from a supermassive black hole

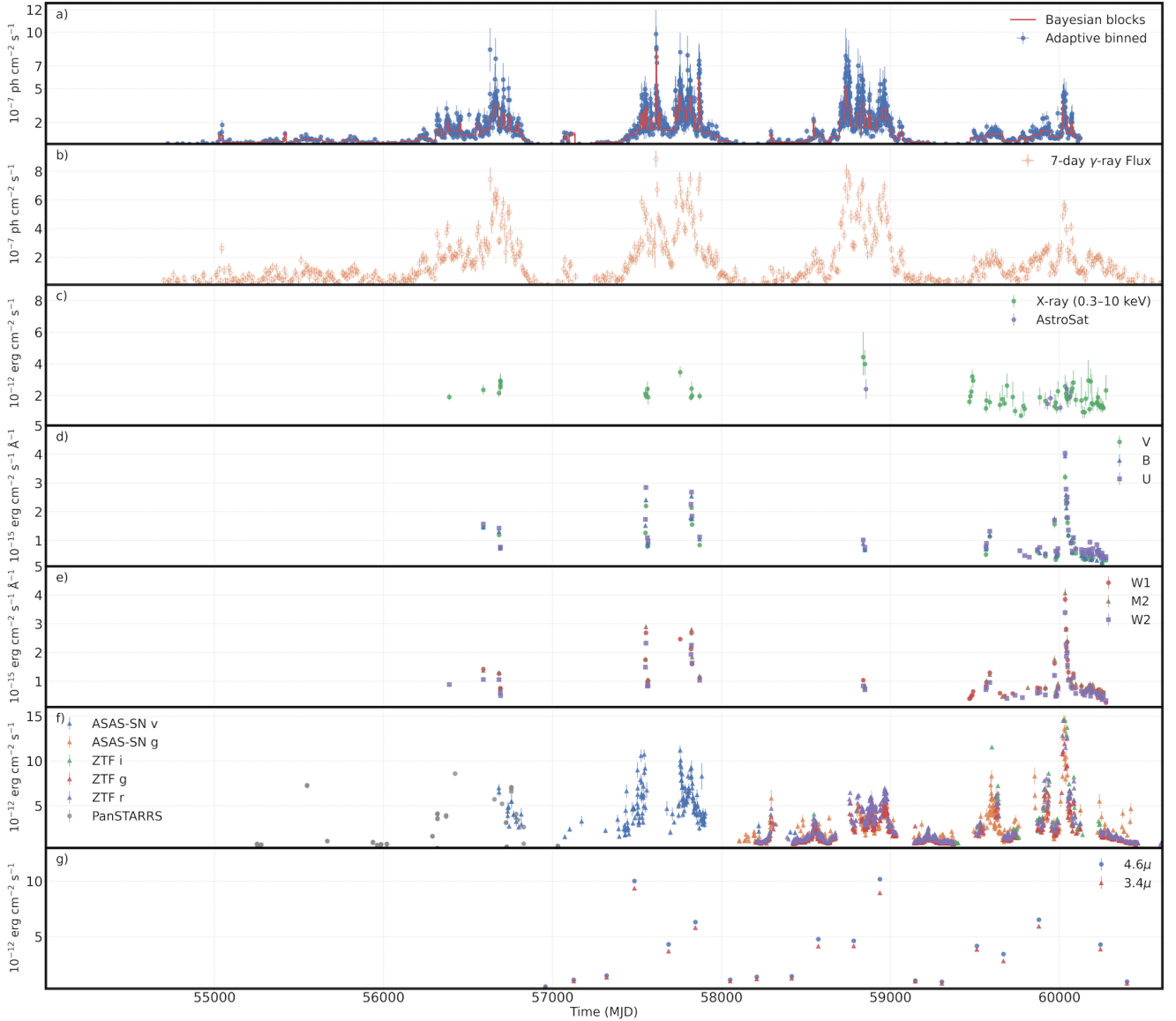


Figure 1: MWL light curve of S5 1044+71. From top to bottom: *Fermi*-LAT integral photon flux (100 MeV to 100 GeV) using adaptive binning, and with a fixed 7-day time bin; *Swift*-XRT and *AstroSat* X-ray integral energy flux (0.3 keV to 10 keV); *Swift*-UVOT flux density per filter (split in V,B, and U, and W1, M2, W2, for visibility); optical spectral energy distribution from ASAS-SN, ZTF, and Pan-STARRS; NEOWISE spectral energy distribution at $3.4\mu\text{m}$ and $4.6\mu\text{m}$.

all sources within a 17° radius of the target from the incremental version of the *Fermi*-LAT fourth source catalog (4FGL-DR3; Abdollahi et al. 2022). The spectral parameters of sources within 12° of the target are left as free parameters, while those outside this region are fixed to their catalog values. The model also includes the standard Galactic diffuse emission template `gll_iem_v07` and the isotropic background model `iso_P8R3_SOURCE_V3_v1`¹. The parameter optimization is performed through a maximum-likelihood fit, where the significance of the γ -ray signal is quantified using the test statistic, denoted TS:

$$TS = 2(\ln L_1 - \ln L_0), \quad (1)$$

¹<https://fermi.gsfc.nasa.gov/ssc/data/access/lat/BackgroundModels.html>

where L_1 and L_0 are the likelihood values with and without the source, respectively (Mattox et al., 1996).

The γ -ray emission of S5 1044+71 is investigated using the adaptive binning method (Lott et al., 2012). This approach allows to track the temporal variability of the γ -ray flux with high sensitivity, enabling the detection of even modest flux changes and facilitating the identification of distinct emission states of the source (see, e.g., Rani et al., 2013; Britto et al., 2016; Sahakyan and Gasparyan, 2017; Zargaryan et al., 2017; Baghmanyany et al., 2017; Gasparyan et al., 2018; Sahakyan et al., 2018; Sahakyan, 2021; Sahakyan et al., 2022; Sahakyan and Giommi, 2022). Unlike traditional fixed-binning techniques, the adaptive method determines the time intervals of the light curve such that each bin achieves a predefined flux uncertainty – here set to 20% –

above the optimal energy threshold – $E_{\text{opt}} = 185.6$ MeV in this work. For each interval, an unbinned likelihood analysis is then performed using the previous criteria.

The γ -ray light curve of S5 1044+71 (above 185.6 MeV) computed with the adaptive binning method is shown in panel a) of Figure 1. The source clearly shows strong variability with phases alternating between quiescent states and phases of enhanced activity during the period covered by the dataset. The average flux in the γ -ray band is $2.15 \times 10^{-7} \text{ph cm}^{-2} \text{s}^{-1}$, while during bright states it increases up to a maximum γ -ray flux of $\sim 9.84 \times 10^{-7} \text{ph cm}^{-2} \text{s}^{-1}$, observed on MJD 57612.69. The light curve also reveals several distinct activity cycles. The source initially remains in a low activity state, followed by a pronounced active phase (e.g., between MJD $\sim 56100 - 56800$ and MJD $\sim 57300 - 58000$, each characterized by multiple flares. After these episodes, the source returns to a quiescent state before entering another active period with similarly strong variability. In total, at least four such cycles can be distinguished, each lasting for extended durations when flaring episodes are observed.

In addition to the γ -ray light curve computed with the adaptive binning method, the 7-day binned light curve is also shown in panel b) of Figure 1. These light curves are extracted from the *Fermi*-LAT Light Curve Repository², where we keep only measurements with $TS > 4$ – corresponding to a $\sim 2\sigma$ detection. Although the flux values in this light curve are averaged over 7-day intervals, the overall variability pattern is consistent with that seen in the adaptively binned light curve. In particular, the source exhibits recurrent activity cycles, within which distinct flaring episodes are observed. Together, these two binning approaches provide complementary views of the temporal variability, with adaptive binning highlighting rapid changes and fixed bins confirming the long-term modulation.

2.2. NuSTAR

The *NuSTAR* satellite (Harrison et al., 2013) observed S5 1044+71 in the 3–79 keV energy range on 2023 April 3, with a total exposure of 23.1 ks. The *NuSTAR* observations of S5 1044+71 were retrieved from the MMDC (Sahakyan et al., 2024b). The data are analyzed using the *NuSTAR*_Spectra tool (Middei et al., 2022) which accesses the *NuSTAR* data archive, retrieves the observations, and performs standard data reduction. In particular, the science-ready products are obtained with the *nuproducts* pipeline. Source counts are extracted from a circular region with a radius of $40''$, while background counts are obtained from an annular region centered on the source position. Spectral fitting is performed assuming a power-law model modified by Galactic absorption. The best-fit parameters are derived using the *XSPEC* package (Arnaud, 1996) and the Cash statistic (Cash, 1979). The analysis shows that the flux in the 3–10 keV band is $(1.45 \pm 0.07) \times 10^{-12} \text{erg cm}^{-2} \text{s}^{-1}$, while it is $(2.31 \pm 0.17) \times 10^{-12} \text{erg cm}^{-2} \text{s}^{-1}$ in the 10–30 keV band. The

photon index measured over the *NuSTAR* energy range is $\Gamma = 1.52 \pm 0.09$, indicating a hard X-ray spectrum. This spectral slope is consistent with the rising part of the inverse-Compton component, as commonly observed in FSRQs. The corresponding *NuSTAR* spectrum is shown in the lower panel of Figure 8.

2.3. Swift-XRT

S5 1044+71 has been observed several times by the *Swift* satellite (Gehrels et al., 2004), often in response to bright flaring states seen by *Fermi*-LAT. In addition to these pointed observations, the source is in the field of view of *Swift* observation of the star KELT-24B, targeted to study its exoplanet (Pillitteri et al., 2023). Given that the observations of KELT-24B have very short individual exposures, we stacked the observations taken within a month.

The *Swift*-XRT data (Burrows et al., 2005) are processed using the standard HEASOFT (v.6.34) tools and the most recent CALDB files³. For each observation, the event files are reprocessed with the task *xrtpipeline*, applying the standard screening criteria and generating cleaned event lists and exposure maps. Source and background spectra are extracted from the cleaned event files using circular regions. For each observation, the corresponding ancillary response files (ARF) are generated with *xrtmkarf*, making use of the exposure maps produced with *xrtexpomap*. The appropriate response matrix files (RMF) are taken from CALDB. Given the generally limited photon statistics of individual observations, the spectra are grouped to a minimum number of 5 counts per bin and analyzed using Cash statistics. Spectral fitting is performed in *XSPEC* assuming an absorbed power-law model (TBabs*powerlaw), with the hydrogen column density fixed to the Galactic value along the line of sight ($N_H = 3.92 \times 10^{20} \text{cm}^{-2}$, from HI4PI Collaboration et al., 2016). For observations with sufficient statistics, both the photon index and normalization are left as free parameters during the fit. For the faintest observations, where the two free parameters could not be both meaningfully constrained, the photon index is fixed to 1.5, and only the normalization is fitted. In all cases, the 0.3–10 keV fluxes are derived from the best-fit models, using the flux command in *XSPEC*.

2.4. AstroSat-SXT

The Soft X-ray Telescope (SXT) onboard the *AstroSat* satellite is a CCD imaging instrument with a 2 m focal length, an angular resolution of ~ 2 arcmin, and operating in the 0.3–8 keV energy range (Singh et al., 2017). *AstroSat*-SXT observed S5 1044+71 in photon counting mode as a target-of-opportunity (ToO) in 2020. Following a successful proposal by the authors to a regular announcement of opportunity (AO) call, *AstroSat* observed S5 1044+71 at several epochs in 2022–2023. We processed the data orbit-by-orbit starting from Level-1 products, retrieved from the ISRO Science Data Archive⁴ Each orbit is reduced with *sxtpipeline*

²<https://fermi.gsfc.nasa.gov/ssc/data/access/lat/LightCurveRepository/>

³<https://heasarc.gsfc.nasa.gov/FTP/caldb>

⁴https://astrobrowse.issdc.gov.in/astro_archive/archive/Home.jsp

Table 1

Photometric measurements from archival photographic plates. The telescope names provided in the table are the one provided in the image's header.

Image	Mag	Err	Detection	Band	Time (UTC)	Telescope
038-7169-B	19.7	0.5	visible	g	1996-12-13 11:03:37	Palomar Schmidt
038-7811-R	18.5	0.5	visible	i	1999-04-11 04:22:14	Palomar Schmidt
062-7353-B	20.7	0.5	visible	B	1997-04-08 05:39:21	Palomar Schmidt
062-7750-R	16.0	0.5	visible	l	1998-12-18 11:55:36	Palomar Schmidt
063-7251-B	18.9	0.5	visible	g	1997-03-03 07:52:45	Palomar Schmidt
063-7278-R	18.3	0.5	visible	r	1997-03-09 07:54:09	Palomar Schmidt
05078	>18.5	–	no	B	1955-03-19 20:19:18	PAO Normal astrograph
05522	>18.5	0.5	no	B	1957-03-22 20:17:26	PAO Normal astrograph
10265	–	–	no	–	1974-02-12 23:38:10	PAO Normal astrograph
13734	>17.5	–	no	B	1983-04-09 19:46:44	PAO Normal astrograph
D0121	18.8	0.5	visible	B	1949-04-25 20:08:40	PAO Normal astrograph
D0906	>18.5	–	no	B	1953-04-05 20:46:17	PAO Normal astrograph
E0685	18.5	0.5	visible	R	1953-03-07 06:33:00	Palomar Schmidt 1.2-m
E0714	19.0	0.5	visible	r	1953-04-12 06:40:00	Palomar Schmidt 1.2-m
O0685	18.8	0.5	visible	B	1953-03-07 07:20:00	Palomar Schmidt 1.2-m
O0714	18.7	0.5	visible	V	1953-04-12 06:20:00	Palomar Schmidt 1.2-m

available in the SXT software (AS1SXTLevel2, version 1.4b), and the resulting Level-2 event lists are merged into a single cleaned event file using the SXT event-merger utility (SXTVEMERGER / SXTMerger.jl) provided by the SXT Payload Operation Center⁵. We used XSELECT (version 2.4d) package built-in to HEASoft (version 6.31.1) to extract image, light curves and spectra from the merged event files. A 16 arcmin circular source aperture is set from the SXT `sxtEEFmake` tool that encloses > 95% of the source's pixels. For timing analysis, the 0.3–10.0 keV (to be consistent with the *Swift*-XRT flux measurements) light curves are extracted using a 1-day bin size and are shown in Figure 1, panel c). For spectrum extraction we use the standard deep blank-sky background ("SkyBkg_comb_EL3p5_CL_Rd16p0_v01.pha") recommended for SXT to mitigate the broad point spread function. We generate source-specific ARFs with the `sxtmkarf` tool, and we applied the standard RMF ("sxt_pc_mat_g0to12.rmf"). Each spectrum is grouped to a minimum of 40 counts per bin prior to fitting. The spectra are fitted in XSPEC with the TBabs*powerlaw model, fixing the Galactic N_H ($3.92 \times 10^{20} \text{ cm}^{-2}$) along the line of sight. The spectra from ToO and AO observations are shown in Figure 8.

2.5. *Swift*-UVOT

The *Swift*/UVOT data (Roming et al., 2005) are analyzed using the tool `uvotmaghist`. For each observation and available filter (V, B, U, UVW1, UVM2, and UVW2), source and background regions are defined and kept fixed across all epochs to ensure consistency. The `uvotmaghist` task is run on all available images to extract photometric measurements, producing time-resolved flux densities and associated statistical uncertainties for each filter. The analysis is performed following the standard UVOT prescriptions, and no additional filtering beyond the default quality criteria is applied. The resulting flux densities are extracted from the

output products and converted into physical units, which are then used to build the optical and ultraviolet light curves in Figure 1, and to complement the MWL SED.

2.6. *AstroSat*-UVIT

The UltraViolet Imaging Telescope (UVIT) onboard the *AstroSat* satellite observed the source between December 2022 and April 2023 with the F1 filter (F148W, effective wavelength $\sim 148 \text{ nm}$) of the FUV channel. The Level-1 data are processed with the standard UVIT L2 pipeline (version 6.3) to produce Level-2, astrometrically calibrated images (including drift correction, flat-fielding, and geometric distortion) (Ghosh et al., 2021). Visual inspection of the Level-2 image shows no significant signal above the background at the source position. Consequently, aperture photometry is not performed and the data are not used in this work. As the source is not detected in the FUV F1 band we obtain an upper limit which is consistent with the UVIT sensitivity for the given exposure and filter.

2.7. Archival optical and IR data

In addition to the optical/UV data from *Swift*-UVOT observations of S5 1044+71, complementary optical measurements are available from several wide-field, all-sky survey facilities, including the All-Sky Automated Survey for Supernovae (ASAS-SN; Shappee et al., 2014; Kochanek et al., 2017), the Zwicky Transient Facility (ZTF; Bellm et al., 2019), and the Panoramic Survey Telescope and Rapid Response System (Pan-STARRS1; Chambers et al., 2016). These data are accessible through the MMDC, and the procedures used to retrieve the observations and convert magnitudes into fluxes are described in detail by Sahakyan et al. (2024b).

The long-term optical light curve of S5 1044+71 is shown in panel f) of Figure 1 which combines data from ASAS-SN (V and g filters), ZTF (i, g, and r filters), and Pan-STARRS (g, r, i, z, y; due to the lower number of

⁵www.tifr.res.in/astrosat_sxt

measurements compared to the other telescopes, the Pan-STARRS filters have been merged in the light curve). This long-term optical monitoring reveals pronounced variability, characterized by multiple episodes of enhanced activity. During quiescent states, the optical flux remains at a baseline level of $\sim (2 - 3) \times 10^{-12} \text{ erg cm}^{-2} \text{ s}^{-1}$ while during the highest activity states it increases to values exceeding $10^{-11} \text{ erg cm}^{-2} \text{ s}^{-1}$. The maximum optical flux of $(2.47 \pm 0.07) \times 10^{-11} \text{ erg cm}^{-2} \text{ s}^{-1}$ is observed in the ASAS-SN g band on MJD 60028.5, while a peak flux of $(1.65 \pm 0.02) \times 10^{-11} \text{ erg cm}^{-2} \text{ s}^{-1}$ is recorded in the ZTF r band on MJD 59895.4.

The comparison of the optical light curve (Figure 1, panel f) with the γ -ray light curves (Figure 1, panels a and b) shows that several major optical brightening episodes occur contemporaneously with enhanced γ -ray activity. In particular, the optical brightening observed between MJD ≈ 57000 and 58000 coincides with γ -ray flaring episode, while additional optical active states are observed between MJD ≈ 59500 and 60000 , coincident with γ -ray activity. However, this behavior is not uniform across all activity phases: despite the γ -ray flux reaching a high state during MJD ≈ 58500 to 59000 the optical flux increases only about half of the other active periods. In contrast, during the last γ -ray activity period, which is characterized by a lower γ -ray flux, the optical flux increases much more significantly.

In addition to the optical data, panel g) of Figure 1 presents the infrared (IR) light curve of S5 1044+71 obtained from observations with the Near-Earth Object Wide-field Infrared Survey Explorer (NEOWISE; Mainzer et al., 2011). The data in the $3.4 \mu\text{m}$ and $4.6 \mu\text{m}$ bands are retrieved from MMDC (Sahakyan et al., 2024b). As NEOWISE observes a given sky position for only a few days approximately every six months, the individual observations separated by less than 10 days are stacked in order to improve the signal-to-noise ratio. Although the IR light curve does not provide continuous monitoring comparable to the γ -ray and optical light curves, it nevertheless shows that the IR flux increases during the γ -ray flaring periods. In the baseline state, the IR flux is at a level of $\sim 2 \times 10^{-12} \text{ erg cm}^{-2} \text{ s}^{-1}$, while during the γ -ray brightening periods it increases up to $\sim 10^{-11} \text{ erg cm}^{-2} \text{ s}^{-1}$.

2.8. Historical optical observations: Palomar and Pulkovo

We analyse archival photographic material from the Palomar and Pulkovo observatories covering the period 1949–1999 provided by the Naroo digitization program (Robert et al., 2021). The dataset consists of scanned photographic plates in which the target S5 1044+71 is present within the field of view. A total of 25 images are available; however, only 15 frames were deemed suitable for photometric analysis. We used Astrometry.net (Lang et al., 2010) to estimate the astrometric solution of the frames. Photometric measurements are obtained using the STDweb⁶ tool (Karpov, 2025), which estimates source magnitudes by comparing the

measured fluxes of objects in the field with reference sources from photometric catalogues. We estimate the photometric calibration against the Pan-STARRS objects (Chambers et al., 2016) and used the conversion relations implemented in the STDweb⁷ code to go from the Pan-STARRS photometric system (where the photometric bands are denoted with g , r , i and z) to the Johnson-Cousins one (where the bands are denoted B , V , R , and I). To estimate the most appropriate band for the calibration of the images, we used the color-term diagnostic tool that had the minimum color-term. The final photometric measurements are reported in Table 1. For the image 10265 in Table 1, we do not find a proper photometric calibration, preventing to have an estimation of S5 1044+71 magnitude, however, a visual inspection of the frame at the AGN’s position reveal no visible source. The same visual inspection reveals no significant excess in the images 05078, 05522, 13734 and D0906, but a photometric calibration is found, allowing for an estimation of upper-limits for S5 1044+71’s luminosity. The latter are estimated by using the background noise inside the aperture multiplied by five times the signal to noise ratio.

3. Variability studies

3.1. Spectral variability

In addition to flux variability, the long-term monitoring of S5 1044+71 enables us to investigate spectral changes within individual bands, and to test whether the source exhibits systematic *harder-when-brighter* or *softer-when-brighter* trends. For the *Fermi*-LAT and the X-ray band, we extract directly the best-fit photon indexes (Γ_γ and Γ_X), and the integral fluxes (F_γ and F_X). For UV/optical we perform a fit of the UVOT flux points only for the observations that contain all available filters, obtaining Γ_{UVOT} , and the integral of the power-law over the UVOT spectral band, F_{UV} . For each band, we quantify spectral variability by fitting the photon index Γ as a function of the logarithm of the flux F :

$$\Gamma = \beta \log_{10}(F) + \delta. \quad (2)$$

When computing the fit, we only use measurements with positive flux and well-defined logarithmic errors, requiring in particular $(F - \sigma_F) > 0$. Pearson correlation coefficients are also reported in Figure 3.1.

The LAT band shows a clear spectral trend with flux: Γ_γ decreases as the γ -ray flux increases, as visible in the top panel of Fig. 3.1, which corresponds to a harder spectrum during bright states. Fitting Γ_γ as a function of $\log_{10}(F_\gamma)$ yields a negative slope with $\beta_\gamma = -0.363 \pm 0.015$, with Pearson $r = -0.626$. In the X-ray band, we also find evidence for spectral variability correlated with flux as Γ_X decreases for increasing X-ray flux, with $\beta_X = -1.42 \pm 0.34$, with Pearson $r = -0.591$. This also indicates a *harder-when-brighter* trend, although the scatter is larger than in the LAT band.

In contrast, the UV/optical proxy displays the opposite tendency as visible in the bottom panel of Fig. 3.1. The

⁶<http://stdweb.favor2.info/>

⁷github.com/karpov-sv/stdpipe/blob/master/stdpipe/catalogs.py

UV/optical index increases with increasing UV/optical flux, corresponding to a softer spectrum in brighter optical/UV states: $\beta_{UVOT} = 0.37 \pm 0.11$ with Pearson $r = 0.537$. This behavior is naturally expected if the observed UV flux includes multiple components with distinct variability properties, for instance a relatively stable thermal contribution from the accretion disk and a variable synchrotron component from the jet.

3.2. Multi-wavelength correlations

To characterize the MWL behavior of the source, we build correlation diagrams between the *Fermi*-LAT light curve and each MWL band. For the optical filters shared between multiple instruments (i.e. g and V), we merged them into a single light curve. We first worked with integral fluxes in X-ray ($F_X[0.3 - 10 \text{ keV}]$) and γ -ray ($F_\gamma[0.1 - 100 \text{ GeV}]$). For optical/infrared data, that are measured from a narrow filter, we use their $\nu F_{\nu,band}$ value. For each MWL band, we associated every *Fermi*-LAT bin with the closest quasi-simultaneous measurement within a maximum time lag of 3.5 days (i.e. half of the width of a γ -ray bin). Given that the same *Fermi*-LAT bin might then be associated with multiple MWL flux points, we explicitly prevented this double counting by creating in these cases an average MWL flux value.

We then fit the correlations with a power-law function:

$$\nu F_{\nu,band} \text{ or } F_X[0.3-10\text{keV}] = b_{PL} \times (F_\gamma[0.1-100\text{GeV}])^{a_{PL}} \quad (3)$$

The results of the fit are shown in Fig. 3 and Table 2. In some of the plots (i.e. r, g), there is evidence for a deviation from this simple power-law. We test for this behavior by adding a constant to the power-law:

$$\nu F_{\nu,band} \text{ or } F_X[0.3-10\text{keV}] = C_{add} + b_{add} \times (F_\gamma[0.1-100\text{GeV}])^{a_{add}} \quad (4)$$

This additional constant can represent a quasi-steady component (e.g. host galaxy, the accretion disk, or emission from the extended jet) on top of the variable jet contribution. In Fig. 3 we show this alternative fit only when it improves significantly over the simpler powerlaw fit.

Because integral quantities can mix flux variability with spectral variability that is present in the data, as presented in the previous Section, we repeated this method using pivot-energy proxies, namely $\nu F_{\nu,1\text{GeV}}$ for *Fermi*-LAT, and $\nu F_{\nu,1.6\text{keV}}$ for *Swift*-XRT and *AstroSat*. The choice of 1 GeV and 1.6 keV as pivot-energies is made considering that these values are close to the typical decorrelation energy, where the flux estimate is least sensitive on the spectra hypothesis. The optical/UV bands are unchanged.

Besides the fact that this choice reduces the dependence on the LAT bandpass integration and on possible photon-index fluctuations, this analysis produces results that are easier to interpret from a theoretical point of view. It is in

fact well known that for synchrotron and synchrotron-self-Compton (SSC) radiation, the SED at a given frequency ν_0 , varies as the Doppler factor to the power of $3 + \alpha_{\nu_0}$ such that:

$$\nu F_\nu \propto \delta^{3+\alpha_{\nu_0}}, \quad (5)$$

where α is the photon index. If the radiation is produced via external-inverse-Compton (EIC) on a target photon field that is boosted into the jet, the dependency becomes:

$$\nu F_\nu \propto \delta^{4+2\alpha_{\nu_0}}. \quad (6)$$

Assuming that a variation in the Doppler factor is at the origin of the variability, MWL correlations naturally emerge because every band responds coherently to the same varying δ . Assuming that the γ -ray emission is due to EIC, and all other bands are due to synchrotron or SSC, the correlation coefficient is thus predicted to be equal to $(3 + \alpha_{band}) / (4 + 2\alpha_{LAT})$. Using average values of $\alpha_{LAT} = 2.2$, $\alpha_X = 1.5$, and $\alpha_{UVOT} = 2.9$, we thus expect a correlation between X-ray and LAT with an index of about 0.7, and between UVOT filters and LAT with an index of about 0.95.

3.3. Time-lags

The correlation study presented above is limited by the fact that it assumes that there is no time-lag between the MWL bands we study. To further investigate this option, we performed a cross-correlation analysis of the *Fermi*-LAT light curve with each MWL light curve. Given the strongly uneven sampling of the data and the heterogeneous cadence across instruments, standard cross-correlation techniques based on regularly sampled time series are not applicable. We therefore adopted the z-transformed discrete correlation function (ZDCF, Alexander, 1997), which is specifically designed to handle sparsely and irregularly sampled light curves. For each MWL band, we computed the ZDCF between the LAT integral flux light curve and the corresponding band-integrated flux. Positive time lags are defined such that the MWL band follows the γ -ray emission. The maximum lag range was chosen to be ± 400 days, ensuring sufficient coverage to probe both short and long delays while preserving adequate statistics in each lag bin. Each ZDCF bin was required to contain a minimum number of 30 data pairs to ensure robust error estimates. This last constrain prevents us to use NEOWISE measurements for this analysis. To assess the statistical significance of the observed ZDCF features, we estimated confidence intervals through a Monte Carlo reshuffling procedure. For each band, we generated 5000 realizations by randomly permuting the flux values of the MWL light curve while keeping the observation times fixed. The ZDCF was recomputed for each surrogate dataset, allowing us to derive empirical confidence envelopes corresponding to the 1σ , 2σ , and 3σ levels under the null hypothesis of no correlation.

Figure 5 shows the resulting ZDCF functions for all considered bands, together with the confidence regions derived

Band	r_p	p_p	r_s	p_s	a_{pl}	b_{pl}	a_{add}	b_{add}	C_{add}	$\Delta\chi^2$	$p(\Delta\chi^2)$
NEOWISE_4.6u	0.83	2.15×10^{-4}	0.83	2.51×10^{-4}	1.06 ± 0.23	-0.83 ± 2.20	–	–	–	–	–
NEOWISE_3.4u	0.84	1.47×10^{-4}	0.83	2.51×10^{-4}	0.99 ± 0.21	-1.44 ± 2.01	–	–	–	–	–
ZTF_i	0.85	8.72×10^{-26}	0.81	1.48×10^{-21}	1.25 ± 0.08	1.03 ± 0.84	–	–	–	–	–
ZTF_r	0.65	1.85×10^{-18}	0.85	3.25×10^{-40}	0.89 ± 0.07	-2.75 ± 0.64	1.36 ± 0.19	$(0.77 \pm 3.25) \times 10^2$	$(8.03 \pm 1.51) \times 10^{-13}$	62.1	3.27×10^{-15}
V (UVOT+ASAS)	0.56	3.12×10^{-9}	0.71	8.68×10^{-16}	0.78 ± 0.08	-3.83 ± 0.78	1.91 ± 0.45	$(0.12 \pm 1.21) \times 10^8$	$(1.69 \pm 0.30) \times 10^{-13}$	98.5	3.21×10^{-23}
g (ASAS+ZTF)	0.64	1.12×10^{-21}	0.79	4.66×10^{-39}	0.90 ± 0.06	-2.78 ± 0.63	1.34 ± 0.17	$(0.40 \pm 1.53) \times 10^2$	$(7.11 \pm 1.17) \times 10^{-13}$	97.1	6.50×10^{-23}
UVOT_bb	0.48	1.17×10^{-3}	0.68	5.17×10^{-7}	1.10 ± 0.19	-0.78 ± 1.84	–	–	–	–	–
UVOT_uu	0.51	2.60×10^{-4}	0.65	7.24×10^{-7}	1.07 ± 0.18	-1.08 ± 1.75	–	–	–	–	–
UVOT_w1	0.58	1.09×10^{-5}	0.69	4.45×10^{-8}	0.89 ± 0.13	-2.91 ± 1.25	1.35 ± 0.31	$(0.38 \pm 2.62) \times 10^2$	$(7.91 \pm 2.75) \times 10^{-13}$	41.0	1.53×10^{-10}
UVOT_m2	0.60	4.23×10^{-5}	0.61	3.46×10^{-5}	0.99 ± 0.17	-2.03 ± 1.64	1.42 ± 0.48	$(0.15 \pm 1.59) \times 10^3$	$(9.28 \pm 4.36) \times 10^{-13}$	20.2	7.01×10^{-6}
UVOT_w2	0.52	1.69×10^{-4}	0.61	5.49×10^{-6}	1.02 ± 0.18	-1.86 ± 1.71	–	–	–	–	–
XRT+SXT	0.48	1.14×10^{-4}	0.39	2.53×10^{-3}	0.21 ± 0.05	-9.64 ± 0.46	–	–	–	–	–

Table 2

Results from the MWL correlations with respect to the integral γ -ray photon flux between 100 MeV and 100 GeV. We provide the Pearson coefficient r_p with its probability p_p , the Spearman coefficient r_s with its probability p_s , the best-fit values for the power-law fit, and the best-fit values for the fit of a power-law with a constant (the latter only when it is favored by $p < 10^{-3}$).

Band	r_p	p_p	r_s	p_s	a_{pl}	b_{pl}	a_{add}	b_{add}	C_{add}	$\Delta\chi^2$	$p(\Delta\chi^2)$
NEOWISE_4.6u	0.844	7.54×10^{-5}	0.832	1.19×10^{-4}	1.04 ± 0.18	-0.28 ± 1.90	–	–	–	–	–
NEOWISE_3.4u	0.854	5.06×10^{-5}	0.843	7.97×10^{-5}	0.97 ± 0.16	-0.98 ± 1.70	–	–	–	–	–
ZTF_i	0.848	2.45×10^{-24}	0.792	2.71×10^{-19}	1.33 ± 0.09	2.84 ± 0.91	–	–	–	–	–
ZTF_r	0.669	2.22×10^{-19}	0.861	4.26×10^{-42}	1.01 ± 0.08	-0.86 ± 0.88	1.46 ± 0.17	$8.71 \times 10^2 \pm 3.55 \times 10^4$	$8.83 \times 10^{-13} \pm 1.11 \times 10^{-13}$	47.11	6.71×10^{-12}
OPT_V (UVOT+ASAS)	0.584	6.30×10^{-10}	0.706	1.84×10^{-15}	0.90 ± 0.10	-2.04 ± 1.02	1.68 ± 0.35	$1.01 \times 10^6 \pm 8.38 \times 10^6$	$1.78 \times 10^{-12} \pm 3.22 \times 10^{-13}$	78.77	6.99×10^{-19}
OPT_g (ASAS+ZTF)	0.633	7.70×10^{-21}	0.776	2.76×10^{-36}	1.08 ± 0.09	-0.25 ± 0.94	1.38 ± 0.16	$1.11 \times 10^3 \pm 4.40 \times 10^3$	$7.42 \times 10^{-13} \pm 1.27 \times 10^{-13}$	74.38	6.45×10^{-18}
UVOT_bb	0.513	4.36×10^{-4}	0.672	8.11×10^{-7}	1.22 ± 0.24	1.31 ± 2.44	–	–	–	–	–
UVOT_uu	0.536	1.02×10^{-4}	0.643	1.11×10^{-6}	1.22 ± 0.23	1.27 ± 2.36	1.83 ± 0.66	$4.80 \times 10^7 \pm 7.51 \times 10^8$	$1.23 \times 10^{-12} \pm 5.74 \times 10^{-13}$	16.66	4.48×10^{-5}
UVOT_w1	0.597	9.56×10^{-6}	0.655	5.75×10^{-7}	1.01 ± 0.16	-1.10 ± 1.64	–	–	–	–	–
UVOT_m2	0.622	2.41×10^{-5}	0.602	5.03×10^{-5}	1.15 ± 0.21	0.37 ± 2.21	1.56 ± 0.53	$4.26 \times 10^4 \pm 5.37 \times 10^5$	$9.15 \times 10^{-13} \pm 4.40 \times 10^{-13}$	20.26	6.77×10^{-6}
UVOT_w2	0.547	6.91×10^{-5}	0.595	1.03×10^{-5}	1.14 ± 0.21	0.11 ± 2.16	–	–	–	–	–
XRT+XRT_1.6keV	0.619	2.84×10^{-7}	0.503	6.69×10^{-5}	0.32 ± 0.05	-8.94 ± 0.52	–	–	–	–	–

Table 3

Results from the MWL correlations with respect to the γ -ray spectral energy distribution evaluated at 1 GeV. We provide the Pearson coefficient r_p with its probability p_p , the Spearman coefficient r_s with its probability p_s , the best-fit values for the power-law fit, and the best-fit values for the fit of a power-law with a constant (the latter only when it is favored by $p < 10^{-3}$).

from the reshuffled realizations. In all optical/UV bands, the ZDCF displays a broad positive peak centered around zero lag, exceeding the 3σ curve, consistent with the strong flux–flux correlations discussed in the previous section. In contrast, X-ray show a flatter ZDCF profiles with larger uncertainties, which is more difficult to interpret. Overall, this analysis suggests that the MWL variability of S5 1044+71 is largely contemporaneous within the temporal resolution of the available data, and does not provide evidence for significant systematic delays between the γ -ray and lower-energy bands.

3.4. Periodicity searches

For the QPO search in the γ -ray light curve, we follow the same approach as the one described in Ren et al. (2023), using the new *Fermi*-LAT data. The Python package PyCWT developed by Torrence and Compo (1998) is used to apply the Continuous Wavelet Transform (CWT) on the light curve. This technique can measure not only the potential constant QPOs, but also the transient and varying periodicities. We use the Morlet wavelet (see equation 1 in Torrence and Compo (1998)) as the mother wavelet, and the source’s light curve is convolved with the translation and dilation of the wavelet function to produce the wavelet power spectrum as presented in the bottom-left panel of Fig. 6). The shaded area in the wavelet spectrum is the cone of influence (COI) where the border effects become important. The Global wavelet spectrum, presented in the right panel of Fig. 6, is the time-averaged wavelet spectrum and corresponds to the true power spectrum of the light curve.

To estimate the significance of the wavelet spectrum and its post-trial significance, we follow the same method as described in Section 4.2 of Ren et al. (2023). We simulated 10^4 fake light curves using the algorithm from Emmanoulopoulos et al. (2013), with the Python implementation provided by Connolly (2015). The latter produces artificial time series with the same statistical and variability properties as the original light curve of S5 1044+71, meaning that the simulated light curves have the same probability distribution function (PDF) and power spectral density (PSD). The confidence levels are then obtained from the histogram of the global wavelet spectrum of all artificial light curves. The post-trial probability is calculated as follows:

$$P_G = 1 - (1 - P_L^a)^n, \quad (7)$$

with P_L being the pre-trial probability. a and n are specific for each mother wavelet, and in this case, following Auchère et al. (2016)’s parameterization, we have: $a = 0.810 (N_{\text{out}} \delta j)^{0.011}$ and $n = 0.491 (N_{\text{out}} \delta j)^{0.926}$ for the local wavelet spectrum; and $a = 0.805 + 0.45 \times 2^{-S_{\text{out}} \delta j}$ and $n = 1.136 (S_{\text{out}} \delta j)^{1.2}$ for the global wavelet spectrum. The parameters $N_{\text{out}} = 787$ and $S_{\text{out}} = 16$ are respectively the time-period bins and the period bins of the wavelet spectrum outside the COI, where border effects become significant.

Fig. 6 shows the source’s light curve in panel a), its CWT map in panel b), with the significance contour lines already in post-trial, and the global wavelet spectrum in panel c). One can notice that the period at around 1100 days is extremely significant in both the CWT maps and the global

spectrum. After fitting a Gaussian function to the global wavelet spectrum curve, we obtain a period of 1114 ± 213 days, where the uncertainty is calculated as the half of the Full Width at Half Maximum.

4. Modeling of γ -ray light curve

The long-term γ -ray flux variability of S5 1044+71 shown in panels a and b) of Figure 1 and in Figure 6 exhibits pronounced repeating out-bursting periods on year-like timescales. There are several mechanisms that can explain such long-timescale QPOs in blazars, including accretion-disk instabilities, jet-disk coupling, binary supermassive black hole systems, and geometrical effects associated with helical or precessing jets. Geometric models are attractive because they can produce large-amplitude, quasi-periodic flux modulations without requiring strong intrinsic changes in the system. In a helical-jet scenario (e.g., Conway and Murphy, 1993; Villata and Raiteri, 1999; Ostorero et al., 2004; Raiteri et al., 2017), the emitting region follows a curved trajectory, periodically approaching and moving away from the line of sight observer, leading to alternating flux enhancements and dimming. In a jet-precession scenario (e.g., Romero et al., 2000; Stirling et al., 2003; Caproni and Abraham, 2004; Britzen et al., 2023) the entire jet axis undergoes slow precession, causing the angle between the jet velocity and the line of sight to vary periodically. In this work, we focus on the jet precession model to reproduce the repeating outbursts observed in the γ -ray light curve of S5 1044+71. Within this model, the observed flux variability is driven by periodic changes in the viewing angle $\theta(t)$ between the jet axis and the line of sight. This change induces time-dependent Doppler boosting. For a jet moving with bulk Lorentz factor Γ_{bulk} , the Doppler factor is given by

$$\delta(t) = \frac{1}{\Gamma_{\text{bulk}} (1 - \beta \mu(t))}, \quad \beta = \sqrt{1 - 1/\Gamma_{\text{bulk}}^2}, \quad (8)$$

where $\mu(t) = \cos \theta(t)$. When the jet viewing angle is small, even small variations in $\theta(t)$ can result in significant changes in $\delta(t)$, and thus in the observed flux. The jet orientation is defined using the standard precession geometry, where the instantaneous viewing angle is computed as:

$$\mu(t) \equiv \cos \theta(t) = \cos i \cos \psi + \sin i \sin \psi \cos \left[\frac{2\pi(t - t_0)}{P} + \phi \right], \quad (9)$$

where i is the inclination of the precession axis relative to the line of sight, ψ is the half-opening angle of the precession cone, P is the precession period (for the observer, corresponding to an intrinsic period $P_{\text{rest}} = P/(1+z)$ with $z = 1.15$), ϕ is a phase offset and t_0 is a reference epoch. It is important to mention that the function is invariant by swapping i and ψ .

In order to connect Doppler boosting with the observed γ -ray variability, we need to assume a flux scaling as a function of $\delta(t)$ as:

$$F(t) = [F_0 + B(t)] \times \delta(t)^{p(t)}, \quad (10)$$

where F_0 is a constant normalization and $B(t)$ is a low-frequency baseline described by a polynomial function, which takes into account the blazar variability not captured by pure geometrical modulation. The functional form of $p(t)$ depends on the dominant emission mechanism, which in this case is assumed to be external inverse-Compton scattering of external photons. As discussed in the previous Section, in this case νF_ν is proportional to $\delta^{4+2\alpha}$, where α is the energy spectral index ($F_\nu \propto \nu^{-\alpha}$). This scaling also holds for the integrated flux within the LAT energy band, under the assumption that the spectrum does not deviate significantly from a power-law function. Using the standard relation $\alpha = \Gamma_\gamma - 1$, this yields:

$$p(t) = 4 + 2\alpha = 2 + 2\Gamma_\gamma(t), \quad (11)$$

where $\Gamma_\gamma(t)$ is the smoothed photon index in the γ -ray band, inferred from the light curve.

The model depends significantly on Γ_{bulk} , for which we tested eight different values from 5 to 22.5. We fit the γ -ray light curve by sampling the posterior distribution of the nonlinear parameter set $\{i, \psi, P, \phi\}$ using nested sampling. In order to successfully fit the first suppressed maximum in the LAT light curve, we increase the order of the polynomial $B(t)$ up to the eight order. The flux normalization F_0 and the coefficients of $B(t)$ are determined simultaneously within the fit. The best-fit parameters are provided in table 4 for all scanned values of Γ_{bulk} . In the upper panel of Figure 7 we show the result for $\Gamma_{\text{bulk}} = 15$, a value typical for FSRQ modeling (see e.g. Ghisellini and Tavecchio, 2015). The fit yields $i = (0.76 \pm 0.13)^\circ$, $\psi = (3.23 \pm 1.08)^\circ$, $P = (1109.2 \pm 5.7)$ d ($\simeq 3.04$ yr), and $\phi = (11.92 \pm 1.85)^\circ$. As discussed above, the best-fit values of i and ψ can be swapped, resulting in a larger angle to the line-of-sight with smaller precession cone. The inferred minimum angular separation between the line of sight and the precession cone, $\chi_{\text{min}} = |i - \psi| = 2.47^\circ$, is smaller than the characteristic relativistic beaming angle, $1/\Gamma_{\text{bulk}} = 3.82^\circ$, implying that the observer periodically enters the beaming cone. In the same way, the maximum angular separation is larger than the beaming angle, explaining the deep minima. The inferred precessing period $\simeq 3.04$ yr is in the same range as inferred from the previous studies and as estimated from our CWT analysis. The model also allows to compute the Doppler boosting in different periods. The evolution of the Doppler boosting over the time is shown in lower panel of Figure 7. The corresponding maximum Doppler factor reaches $\delta_{\text{max}} \simeq 21.14$ while the lowest is $\delta_{\text{min}} \simeq 14.36$.

5. SED Modeling

The MWL light curves shown in Fig. 1 allow for the identification of several epochs with sufficiently contemporaneous data and for the construction of time-resolved

Table 4

Best-fit parameters of the precessing-jet light-curve model (mode M2, EIC, polynomial order 6) for different assumed bulk Lorentz factors Γ . Quoted uncertainties correspond to posterior standard deviations.

Γ	i (deg)	ψ (deg)	$ i - \psi $ (deg)	P (days)	ϕ (deg)	δ_{\max}	$\ln \mathcal{Z}$
5.0	3.30 ± 0.30	4.32 ± 0.48	1.02	1112.3 ± 5.8	14.3 ± 1.7	9.82	10050.23
7.5	2.02 ± 0.28	3.29 ± 0.65	1.27	1110.4 ± 5.8	13.0 ± 1.6	14.54	10050.86
10.0	1.37 ± 0.25	2.99 ± 0.86	1.62	1109.9 ± 5.8	12.4 ± 1.7	18.49	10049.98
12.5	0.98 ± 0.19	3.09 ± 1.04	2.11	1109.4 ± 5.8	12.2 ± 1.7	20.61	10049.13
15.0	0.76 ± 0.13	3.23 ± 1.08	2.47	1109.2 ± 5.7	11.9 ± 1.9	21.14	10048.74
17.5	0.65 ± 0.11	2.76 ± 1.00	2.10	1108.6 ± 5.9	11.6 ± 2.0	24.78	10047.96
20.0	0.55 ± 0.07	3.38 ± 1.08	2.83	1109.3 ± 6.1	12.1 ± 1.9	20.27	10048.18
22.5	0.50 ± 0.05	3.52 ± 1.19	3.02	1109.4 ± 5.9	12.4 ± 2.1	18.73	10047.25

SEDs suitable for theoretical modeling. Performing SED modeling across distinct periods is essential, as it enables to track changes in the emission components. To reliably constrain both the synchrotron and inverse-Compton emission components, SEDs are constructed only for epochs in which X-ray observations are available. However, as noted in Section 2, the source is relatively faint in the X-ray band, and a single short *Swift*-XRT exposure typically does not provide sufficient signal-to-noise ratio to produce an SED suitable for modeling. Consequently, XRT observations that are close in time and show no evidence of significant variability are merged and re-analyzed. This allows to obtain spectra with adequate photon statistics and to extract a sufficient number of data points for theoretical modeling. Similarly, to improve photon statistics in the HE γ -ray band, the adaptively binned light curve is segmented into intervals of approximately constant flux using the Bayesian Block algorithm (Scargle et al., 2013). Within each block the flux is assumed to be statistically consistent with a constant level, allowing to perform spectral analysis over a longer integration time than one individual measurement and thereby obtain spectra that extend above the GeV band. The resulting Bayesian blocks are shown as red segments in panel a) of Fig. 1. The start and end times of these blocks are then used to search for contemporaneous observations in the other bands, enabling the construction of MWL SEDs based on overlapping time intervals. This procedure follows the SED/light-curve animation method described in Sahakyan et al. (2024b).

Based on this approach, the following intervals defined by the Bayesian-block boundaries are selected for SED modeling. For each period, all available *Swift*-XRT pointings within the corresponding MJD range are merged into a single spectrum after verifying the absence of significant intra-interval variability, and *Swift*-UVOT data are taken from the exposure providing full filter coverage. Specifically:

- *Period (P1)*: MJD 56678.5–56699.8, an interval within the first γ -ray brightening episode. UVOT data are taken from the 26 January 2014 exposure.
- *Period (P2)*: MJD 58827.5–58841.4, within the third γ -ray brightening and overlapping with an *AstroSat* observation in 2020. UVOT data are taken from the 21 December 2019 exposure.

- *Period (P3)*: MJD 60023.0–60045.28, a segment of the fourth γ -ray brightening, coincident with a *NuSTAR* pointing and a second *AstroSat* observation. UVOT data are taken from the 5 April 2023 exposure.

The SED corresponding to the second brightening phase is not modeled, as it is essentially identical to the one observed during the first brightening episode and therefore does not provide additional independent constraints. The three selected intervals represent distinct emission states of the source, and modeling their contemporaneous SEDs allows to obtain meaningful constraints on the evolution of the physical parameters.

5.1. One-zone leptonic external inverse Compton model

The double-peaked SED of FSRQs is commonly interpreted within the external inverse Compton (EIC) scenario, in which relativistic electrons in the jet up-scatter both internally produced synchrotron photons and external radiation fields. The dominant source of external seed photons depends on the location of the emitting region relative to the central black hole. Possible contributors include direct radiation from the accretion disk (Dermer et al., 1992; Dermer and Schlickeiser, 1994), photons reprocessed in the broad-line region (BLR) (Sikora et al., 1994), and infrared emission from the dusty torus (Błażejowski et al., 2000).

The EIC model adopted in this study is based on a convolutional neural network (CNN) surrogate approach that replaces computationally expensive numerical calculations, enabling efficient global inference of the model parameters. A detailed description of the model is provided in Sahakyan et al. (2024a); here we summarize the key aspects.

The emission region is assumed to be a spherical blob of radius R , located at a distance R_{diss} from the central black hole and filled with a uniform magnetic field. The blob moves relativistically along the jet with bulk Lorentz factor Γ ; assuming a small viewing angle, the Doppler factor is $\delta \simeq \Gamma$. Following standard jet geometry, the distance of the dissipation region from the central engine scales with the emission region size as $R_{\text{diss}} \simeq \Gamma R$.

Relativistic electrons are continuously injected into the emitting region according to a power-law distribution with

an exponential cutoff,

$$Q_e(\gamma) = \begin{cases} Q_{e,0} \gamma^{-p} \exp\left(-\frac{\gamma}{\gamma_{\max}}\right), & \gamma \geq \gamma_{\min}, \\ 0, & \text{otherwise,} \end{cases} \quad (12)$$

where p is the electron spectral index, and γ_{\min} and γ_{\max} are the minimum and maximum Lorentz factors, respectively. The normalization $Q_{e,0}$ defines the total electron luminosity given by:

$$L_e = \pi R^2 \delta^2 m_e c^3 \int_1^{\infty} \gamma Q_e(\gamma) d\gamma. \quad (13)$$

External photon fields are modeled following standard prescriptions and include thermal emissions from the accretion disk, radiation reprocessed by the BLR, and infrared emissions from the dusty torus. The latter two components are assumed to scale with the accretion-disk luminosity (L_d). The spectra of the external photon fields are approximated as blackbody distributions, defined in the black hole frame and Lorentz-transformed into the comoving frame of the emitting region. Consequently, the model has nine free parameters: the emitting region radius R , Doppler factor δ , magnetic field strength B , electron luminosity L_e , minimum and maximum electron Lorentz factors γ_{\min} and γ_{\max} , the electron spectral index p , the accretion-disk luminosity L_d , and the black hole mass M_{BH} , which determines the characteristic temperature of the accretion-disk emission. Considering a broad range for these parameters as presented in Table 1 of Sahakyan et al. (2024a), we generate synthetic SEDs with the SOPRANO code (Gasparyan et al., 2022) to generate the training dataset for the CNN. After the training phase, the CNN accurately reproduces the radiative output of the EIC model while reducing the computational cost of generating individual SEDs by orders of magnitude. The trained CNN for the EIC model, together with analogous CNNs developed for synchrotron self-Compton (SSC; Bégué et al. 2024) and lepto-hadronic models (Sahakyan et al., 2025), are publicly available through the MMD platform (Sahakyan et al., 2024b).

5.2. Modeling results

The selected SEDs are modeled by coupling the CNN surrogate with the nested sampling algorithm MultiNest (Feroz et al., 2009), using 1500 live points and a tolerance parameter of 0.4 to ensure efficient sampling and convergence. Due to the lack of low-frequency data ($< 10^{10}$ Hz), the minimum electron Lorentz factor is fixed at $\gamma_{\min} = 100$ for all epochs. For each SED, the Doppler factor is inferred independently from jet precession modeling of the γ -ray light curve, which provides the temporal evolution of δ as well. The value of δ corresponding to the epoch of the *Swift*-UVOT observation is then adopted in the SED modeling for each period; the resulting δ values are reported in Table 5. Absorption by the extragalactic background light (EBL) is included in the model calculations using the model of Domínguez et al. (2011). Other unknown

parameters in the model are the black hole mass and the accretion disk luminosity. When a “blue bump” (Ghisellini et al., 2010) is observed in the optical/UV band, it can be attributed to direct thermal emission from the accretion disk and used to constrain these parameters. However, no such feature is evident in the long-term SED of S5 1044+71. We therefore constrained the accretion disk luminosity and its characteristic temperature (the black hole mass) by fitting a disk component to the full set of optical/UV observations of S5 1044+71, requiring that the disk emission does not exceed the observed lower fluxes. This procedure yields $L_{\text{disk}} = 1.14 \times 10^{46} \text{ erg s}^{-1}$ and $M_{\text{BH}} = 2.6 \times 10^9 M_{\odot}$. It should be noted that the inferred black hole mass is consistent with the value reported in Wang et al. (2025), $M_{\text{BH}} = 3.49 \times 10^9 M_{\odot}$, which was estimated from the observed QPO period. However, the inferred accretion disk luminosity is somewhat higher than the value estimated by Paliya et al. (2021), $L_{\text{disk}} = 1.38 \times 10^{45} \text{ erg s}^{-1}$, which was derived from the luminosity of the BLR. In our modeling, adopting $L_{\text{disk}} = 1.38 \times 10^{45} \text{ erg s}^{-1}$ together with $\delta \simeq 21$ (see Table 5) requires extremely large electron powers, $L_e \gtrsim 10^{48} \text{ erg s}^{-1}$, to reproduce the high γ -ray flux observed during the active periods. Such a scenario is not only problematic from the point of the required jet energetics, but also leads to a regime in which the SSC component dominates over the EIC component. Therefore, the derived disk luminosity used in this work should be considered as an upper limit, which we adopt as the maximum allowed contribution from the accretion disk.

The modeling results of the SEDs for the three active periods (P1–P3) are shown in Figure 8, and the corresponding best-fit parameters are listed in Table 5. The model corresponding to the best-fit parameters is shown as a blue solid line, while the associated model uncertainty is shown in gray. In all three active states, the emission up to the optical/UV band is dominated by synchrotron radiation from relativistic electrons. The X-ray emission is primarily produced via SSC scattering, whereas the HE γ -ray emission is explained by the EIC component. Although the SEDs correspond to different activity states, the derived model parameters do not show significant variations across the three periods. The power-law index of the emitting electron population remains close to ~ 2 in all epochs. The cutoff Lorentz factor shows a modest increase from P1 to P3, with $\log \gamma_{\text{cut}}$ changing from 4.02 to 4.56, indicating that electrons are accelerated to higher maximum energies during the later activity state. The magnetic field strength remains consistent within uncertainties, with $\log B \sim -1.1$ to -1.4 , while the size of the emitting region is also stable, $\log R \simeq 17.6$. The electron power is comparable in P1 and P2, with $\log L_e \simeq 46.48$, and decreases moderately in P3 to $\log L_e \simeq 46.33$. Finally, the magnetic power, computed as $L_B = \pi c R_b^2 \Gamma^2 U_B$, is lower than the electron power in all periods $\log L_B \simeq 44.4 - 45.1$, implying a particle-dominated emitting region during these outburst states.

Table 5

Best-fit parameters of the leptonic emission model for the three activity emission periods (P1–P3) of S5 1044+71. The Doppler factor δ is not a free parameter of the SED fit but is inferred from the jet precession modeling. The minimum electron Lorentz factor was fixed to $\gamma_{\min} = 100$ in all fits. The accretion disk luminosity and black hole mass were also fixed to $L_{\text{disk}} = 1.14 \times 10^{46} \text{ erg s}^{-1}$ and $M_{\text{BH}} = 2.6 \times 10^9 M_{\odot}$, respectively.

Parameter	P1	P2	P3
p	2.02 ± 0.16	2.09 ± 0.17	2.03 ± 0.10
δ	21.04	21.07	20.82
$\log \gamma_{\text{cut}}$	4.02 ± 0.35	4.33 ± 0.33	4.56 ± 0.31
$\log B$	-1.29 ± 0.60	-1.44 ± 0.47	-1.10 ± 0.59
$\log R$	17.57 ± 0.43	17.55 ± 0.27	17.56 ± 0.32
$\log L_e$	46.48 ± 0.54	46.48 ± 0.53	46.33 ± 0.48
$\log L_B$	44.78	44.43	45.13

6. Discussions and Conclusions

In this work we have presented a comprehensive MWL study of the FSRQ S5 1044+71, based on contemporaneous observations covering the full electromagnetic spectrum. At high energies we combined *Fermi*-LAT γ -ray monitoring with X-ray observations from *Swift*-XRT, *AstroSat*-SXT, and *NuSTAR*, while the optical and near-infrared domain is sampled by ZTF, Pan-STARRS, ASAS-SN, and NEOWISE. Archival optical data were also considered to extend the temporal baseline. Although the historical data are too sparse to provide a constraint on the long-term light curve, they show clear variability in optical, with for example a bright flare during December 18, 1998. If we consider the best-fit periodicity of 1110 days, with maxima in the *Fermi* era at around MJD 55550, 56660, 57770, 58880, and 59990, one of the previous maxima happened at MJD 51110, that is less than two months before that Palomar observations. Remarkably, none of the other historical observations are close to a predicted past maximum.

The combined light curves reveal pronounced long-term variability, characterized by four major episodes of enhanced activity on year-long timescales. A time-frequency analysis based on the continuous wavelet transform (CWT), reveals a characteristic timescale of ~ 1100 days. This timescale is also recovered by the LAT light-curve fitting and is further supported by the recurrence of major γ -ray outbursts. The robustness of this timescale points to a genuine long-term modulation.

The long-term variability is accompanied by clear MWL correlations. Strong flux-flux correlations are observed between the γ -ray and optical/UV/IR bands, while correlations involving the X-ray emission are significantly weaker, although it is important to underline that X-ray observations are sparser and biased towards the LAT bright states. The ZDCF analysis indicates that the optical/UV variations are broadly contemporaneous with the γ -ray emission within uncertainties, and no significant time lag is detected. These results suggest that the dominant variability across the optical to γ -ray bands is driven by a common mechanism.

The slopes of the observed flux-flux relations provide important physical constraints. In Sect. 3.2 we introduced the fact that, if long-term variability were dominated by changes in the Doppler factor, the correlation index can be predicted to be of about 0.7 between X-ray and γ -ray, and 0.95 between optical/UV and γ -ray. The values we observe are close to 1 for the latter, while for the X-rays we observe a smaller index of about 0.3. Part of the discrepancy is expected because the simple estimate assumes no spectral variability, which we do observe. In addition, and as mentioned above, the X-ray measurements are not coming from an unbiased monitoring, but are biased towards the LAT flaring states. The correlation study seems to globally support indeed a variability driven by changes in the Doppler factor. But, more interestingly, it can also be used to challenge alternative models. If the periodicity would be due to changes in the particle content in the jet, (i.e. variations of the electron normalization linked to accretion-rate fluctuations), a one-zone leptonic scenario would predict an approximately linear relation between synchrotron (optical) and external inverse-Compton (EIC; γ -ray) emission, and a nearly quadratic response of the SSC-dominated X-rays (again, ignoring here spectral variability as we did for the Doppler-factor variability discussion). This prediction is remarkably different compared to the Doppler factor change: X-rays, being SSC dominated, should have shown a much stronger variability than the other bands. The observed behavior is markedly different: while the optical- γ correlation is close to linear and cannot be used to discriminate between variability processes, the X- γ correlation is much flatter than expected in a particle-driven scenario. This discrepancy strongly disfavors models in which long-term variability is primarily driven by changes in the electron density and thus on the injection of particles in the emitting region.

The spectral variability study further supports the picture of a Doppler-factor induced variability. In addition to the flux brightening, an increase of δ also induces a translation of the SED to higher energies. If the SED peaks are close to the observing bands, the spectral variability is naturally explained. In this scenario, the harder-when-brighter behaviour in LAT data is due to the EIC peak getting closer to the LAT energy band, flattening the broad-band spectrum. In the same way, the harder-when-brighter behaviour in X-ray data is due to the shift to higher energies of the curved low-energy part of the SSC component. The softer-when-brighter behaviour in optical spectra is on the other hand probably due to the emergence of a separate hard component (likely the accretion disk) during the low flux states from the jet. This effect is also supported by the fact that in several of the optical/ γ -ray correlations there is preference for a constant function superposed to the powerlaw correlation.

To investigate the physical origin of the long-term modulation, we modeled the LAT light curve within the framework of a precessing relativistic jet. In this scenario, periodic changes in the angle between the jet axis and the line of sight lead to time-dependent Doppler boosting of the observed emission. Using Bayesian inference, we infer a precession

period of $P \simeq 1109$ d ($\simeq 3.04$ yr), fully consistent with the characteristic timescale identified by the CWT analysis and with the recurrence timescale of the observed outbursts. The best-fit solution corresponds to a strongly aligned geometry, with an inclination $i \simeq 0.76^\circ$ and a precession cone half-opening angle $\psi \simeq 3.23^\circ$, assuming a bulk Lorentz factor of 15 (we note that for the model i and ψ can be inverted). The corresponding Doppler factor varies in the range $\delta \sim 14.4$ to 21.1, which is sufficient to produce large-amplitude flux enhancements even if the comoving emissivity varies only modestly. Importantly, scanning the bulk Lorentz factor over a wide range yields consistent precession periods and similar likelihood values, indicating that the inferred period is data-driven and not an artifact of a particular choice of Γ_{bulk} . We remind the reader that the fitted periodicity does not take into account cosmological redshift. The precessing period in the AGN frame is $P_{\text{rest}} \simeq 1110/2.15 \simeq 516$ days.

The precessing-jet model we present thus provides a natural explanation for all observational features of S5 1044+71: the quasi-regular recurrence of major γ -ray outbursts, the strong optical- γ correlations, and the comparatively weaker X-ray response. In this picture, Doppler-factor variations define the long-term envelope of the variability, while intrinsic changes in the electron distribution and additional emission components modulate the detailed spectral and temporal behavior.

We modeled the spectral energy distribution of S5 1044+71 during three distinct activity states using a one-zone leptonic EIC framework, implemented through a CNN-based surrogate coupled with MultiNest to efficiently explore the high-dimensional parameter space. The fits indicate an electron energy distribution with a power-law index $p \simeq 2$, consistent with standard diffusive shock acceleration. The cutoff Lorentz factor spans $\gamma_{\text{cut}} \sim (1\text{--}3.6) \times 10^4$, with a modest increase toward the latest activity state, suggesting either more efficient acceleration or reduced radiative constraints during that epoch.

Despite the different activity levels, the inferred physical conditions of the emitting region remain remarkably stable. Both the magnetic field strength and the size of the emission region are consistent within uncertainties across P1–P3. This implies that the outbursts are not driven by large-scale structural changes of the emission zone, but rather by variations in the high-energy tail and normalization of the electron population, combined with geometric Doppler modulation.

The SED modeling also provides constraints on the location of the emission region. In the adopted framework, the emitting-region size and distance along the jet are related through $R_{\text{diss}} \simeq \Gamma R$. The inferred size, $\log R \simeq 17.6$, together with $\delta \simeq \Gamma \simeq 21$, places the dissipation region at $R_{\text{diss}} \gtrsim 10^{18}$ cm from the central black hole. For the inferred accretion-disk luminosity $L_{\text{disk}} = 1.14 \times 10^{46}$ erg s $^{-1}$, the expected BLR radius is $R_{\text{BLR}} \simeq 3.4 \times 10^{17}$ cm, implying that the emission region is located well outside the BLR. In this regime, the dominant external photon field for inverse Compton scattering is provided by the dusty torus rather than the BLR. This configuration reduces internal $\gamma\gamma$ absorption

and makes S5 1044+71 a plausible candidate for very-high-energy γ -ray emission during bright states. The redshift of the source ($z = 1.15$) is larger than the current most-distant very-high-energy blazars (H. E. S. S. Collaboration et al., 2026; Cortina and CTAO LST Collaboration, 2023), but it is reachable by CTAO. The predictability of the flaring activity from S5 1044+71 can make it an important target to study propagation of very-high-energy γ -ray photons on cosmological distances.

The detection of a stable, year-scale modulation naturally raises the question of its physical origin. Precession of the jet-launching region can arise from several mechanisms, including warped or tilted accretion disks (Caproni et al., 2004; Liska et al., 2018), or tidal torques in a black hole binary (Larwood, 1998). Our geometric modeling constrains the effective precession parameters but does not, by itself, uniquely identify the underlying physical driver.

Recent works (Kun et al., 2022, 2024) have proposed that the long-term modulation in S5 1044+71 may be linked to spin-orbit precession in a very compact, near-merger SMBH binary. In such scenarios, year-scale precession of the black hole spin becomes possible because relativistic spin-orbit torques grow rapidly in the late inspiral phase. While our results are compatible with such an interpretation, they do not require it. We do not observe any evidence for deviation from the $P \simeq 1100$ days period, not in the CWT analysis (that is sensitive to QPO with shifting period), nor in the light-curve fit. In addition, a near-merger binary would plausibly perturb the broad-line region, potentially producing asymmetric or time-variable line profiles. Optical spectra of S5 1044+71, including archival Steward Observatory data⁸, appear consistent with those of a standard FSRQ and do not show obvious signatures of strong BLR disruption. This does not exclude a compact binary configuration, but it requires that the BLR is not affected by it. An alternative possibility is that the precession involves the inner accretion flow or jet-launching region rather than the black hole spin itself. In this case, a misalignment between the disk angular momentum and the black hole spin can lead to a precessing jet nozzle without invoking a near-coalescence binary. Such a scenario naturally explains the modest precession cone angle inferred from the light-curve modeling and is consistent with the absence of clear spectroscopic anomalies.

In summary, our MWL analysis of S5 1044+71 reveals a robust, long-term modulation with a characteristic timescale of ~ 3 yr, accompanied by strong optical- γ correlations and weaker X-ray variability. Flux-flux correlations disfavor particle-content-driven scenarios and instead support a geometric Doppler-factor modulation as the dominant driver of the long-term variability. A precessing-jet model provides a self-consistent description of the long-term *Fermi*-LAT light curve, of the spectral variability observed in γ -rays, X-rays, and optical, of the flux-flux correlations, and of the absence of time-lags between bands. The SED modeling places the

⁸see <https://james.as.arizona.edu/~psmith/Fermi/>

emission region beyond the BLR and supports an EIC-dominated high-energy component, making this object an interesting target for very-high-energy γ -ray observations.

Future progress will require continued long-term monitoring to test the phase stability of the modulation over additional cycles, as well as high-resolution VLBI observations to directly probe changes in jet orientation. Dedicated spectroscopic monitoring of the broad emission lines could provide an independent test of compact-binary scenarios. Based on our best-fit model of the *Fermi*-LAT light curve, the next maximum is expected during March 2026. Given the broadness of the activity period, high γ -ray state is expected for few months before and after.

References

- Abdollahi, S., Acero, F., Baldini, L., Ballet, J., Bastieri, D., Bellazzini, R., Berenji, B., Berretta, A., Bissaldi, E., Blandford, R.D., Bloom, E., Bonino, R., Brill, A., Britto, R.J., Bruel, P., Burnett, T.H., Buson, S., Cameron, R.A., Caputo, R., Caraveo, P.A., Castro, D., Chaty, S., Cheung, C.C., Chiaro, G., Cibrario, N., Ciprini, S., Coronado-Blázquez, J., Crnogorčević, M., Cutini, S., D'Ammando, F., De Gaetano, S., Digel, S.W., Di Lalla, N., Dirirsa, F., Di Venere, L., Domínguez, A., Fallah Ramazani, V., Fegan, S.J., Ferrara, E.C., Fiori, A., Fleischhack, H., Franckowiak, A., Fukazawa, Y., Funk, S., Fusco, P., Galanti, G., Gammaldi, V., Gargano, F., Garrappa, S., Gasparrini, D., Giacchino, F., Giglietto, N., Giordano, F., Giroletti, M., Glanzman, T., Green, D., Grenier, I.A., Grondin, M.H., Guillemot, L., Guiriec, S., Gustafsson, M., Harding, A.K., Hays, E., Hewitt, J.W., Horan, D., Hou, X., Jóhannesson, G., Karwin, C., Kayanoki, T., Kerr, M., Kuss, M., Landriu, D., Larsson, S., Latronico, L., Lemoine-Goumard, M., Li, J., Liodakis, I., Longo, F., Loparco, F., Lott, B., Lubrano, P., Maldera, S., Malyshev, D., Manfreda, A., Martí-Devesa, G., Mazziotta, M.N., Mereu, I., Meyer, M., Michelson, P.F., Mirabal, N., Mitthumsiri, W., Mizuno, T., Moiseev, A.A., Monzani, M.E., Morselli, A., Moskalenko, I.V., Negro, M., Nuss, E., Omodei, N., Orienti, M., Orlando, E., Paneque, D., Pei, Z., Perkins, J.S., Persic, M., Pesce-Rollins, M., Petrosian, V., Pillera, R., Poon, H., Porter, T.A., Principe, G., Rainò, S., Rando, R., Rani, B., Razzano, M., Razaque, S., Reimer, A., Reimer, O., Reposeur, T., Sánchez-Conde, M., Saz Parkinson, P.M., Scotton, L., Serini, D., Sgrò, C., Siskind, E.J., Smith, D.A., Spandre, G., Spinelli, P., Sueoka, K., Suson, D.J., Tajima, H., Tak, D., Thayer, J.B., Thompson, D.J., Torres, D.F., Troja, E., Valverde, J., Wood, K., Zaharijas, G., 2022. Incremental Fermi Large Area Telescope Fourth Source Catalog. *ApJS* 260, 53. doi:10.3847/1538-4365/ac6751, arXiv:2201.11184.
- Ackermann, M., Ajello, M., Albert, A., Atwood, W.B., Baldini, L., Ballet, J., Barbiellini, G., Bastieri, D., Becerra Gonzalez, J., Bellazzini, R., Bissaldi, E., Blandford, R.D., Bloom, E.D., Bonino, R., Bottacini, E., Bregeon, J., Bruel, P., Buehler, R., Buson, S., Caliandro, G.A., Cameron, R.A., Caputo, R., Caragiulo, M., Caraveo, P.A., Cavazzuti, E., Cecchi, C., Chekhtman, A., Chiang, J., Chiaro, G., Ciprini, S., Cohen-Tanugi, J., Conrad, J., Cutini, S., D'Ammando, F., de Angelis, A., de Palma, F., Desiante, R., Di Venere, L., Domínguez, A., Drell, P.S., Favuzzi, C., Fegan, S.J., Ferrara, E.C., Focke, W.B., Fuhrmann, L., Fukazawa, Y., Fusco, P., Gargano, F., Gasparrini, D., Giglietto, N., Giommi, P., Giordano, F., Giroletti, M., Godfrey, G., Green, D., Grenier, I.A., Grove, J.E., Guiriec, S., Harding, A.K., Hays, E., Hewitt, J.W., Hill, A.B., Horan, D., Jogler, T., Jóhannesson, G., Johnson, A.S., Kamae, T., Kuss, M., Larsson, S., Latronico, L., Li, J., Li, L., Longo, F., Loparco, F., Lott, B., Lovellette, M.N., Lubrano, P., Magill, J., Maldera, S., Manfreda, A., Max-Moerbeck, W., Mayer, M., Mazziotta, M.N., McEnery, J.E., Michelson, P.F., Mizuno, T., Monzani, M.E., Morselli, A., Moskalenko, I.V., Murgia, S., Nuss, E., Ohno, M., Ohsugi, T., Ojha, R., Omodei, N., Orlando, E., Ormes, J.F., Paneque, D., Pearson, T.J., Perkins, J.S., Perri, M., Pesce-Rollins, M., Petrosian, V., Piron, F., Pivato, G., Porter, T.A., Rainò, S., Rando, R., Razzano, M., Readhead, A., Reimer, A., Reimer, O., Schulz, A., Sgrò, C., Siskind, E.J., Spada, F., Spandre, G., Spinelli, P., Suson, D.J., Takahashi, H., Thayer, J.B., Thompson, D.J., Tibaldo, L., Torres, D.F., Tosti, G., Troja, E., Uchiyama, Y., Vianello, G., Wood, K.S., Wood, M., Zimmer, S., Berdyugin, A., Corbet, R.H.D., Hovatta, T., Lindfors, E., Nilsson, K., Reinthal, R., Sillanpää, A., Stamerra, A., Takalo, L.O., Valtonen, M.J., 2015. Multiwavelength Evidence for Quasi-periodic Modulation in the Gamma-Ray Blazar PG 1553+113. *ApJ* 813, L41. doi:10.1088/2041-8205/813/2/L41, arXiv:1509.02063.
- Alexander, T., 1997. Is AGN Variability Correlated with Other AGN Properties? ZDCF Analysis of Small Samples of Sparse Light Curves, in: Maoz, D., Sternberg, A., Leibowitz, E.M. (Eds.), *Astronomical Time Series*, p. 163. doi:10.1007/978-94-015-8941-3_14.
- Arnaud, K.A., 1996. XSPEC: The First Ten Years, in: Jacoby, G.H., Barnes, J. (Eds.), *Astronomical Data Analysis Software and Systems V*, p. 17.
- Atwood, W.B., Abdo, A.A., Ackermann, M., Althouse, W., Anderson, B., Axelsson, M., Baldini, L., Ballet, J., Band, D.L., Barbiellini, G., Bartelt, J., Bastieri, D., Baughman, B.M., Bechtol, K., Bédérède, D., Bellardi, F., Bellazzini, R., Berenji, B., Bignami, G.F., Bisello, D., Bissaldi, E., Blandford, R.D., Bloom, E.D., Bogart, J.R., Bonamente, E., Bonnell, J., Borgland, A.W., Bouvier, A., Bregeon, J., Brez, A., Brigida, M., Bruel, P., Burnett, T.H., Busetto, G., Caliandro, G.A., Cameron, R.A., Caraveo, P.A., Carius, S., Carlson, P., Casandjian, J.M., Cavazzuti, E., Ceccanti, M., Cecchi, C., Charles, E., Chekhtman, A., Cheung, C.C., Chiang, J., Chipaux, R., Cillis, A.N., Ciprini, S., Claus, R., Cohen-Tanugi, J., Condamore, S., Conrad, J., Corbet, R., Corucci, L., Costamante, L., Cutini, S., Davis, D.S., Decotigny, D., DeKlotz, M., Dermer, C.D., de Angelis, A., Digel, S.W., do Couto e Silva, E., Drell, P.S., Dubois, R., Dumora, D., Edmonds, Y., Fabiani, D., Farnier, C., Favuzzi, C., Flath, D.L., Fleury, P., Focke, W.B., Funk, S., Fusco, P., Gargano, F., Gasparrini, D., Gehrels, N., Gentit, F.X., Germani, S., Giebels, B., Giglietto, N., Giommi, P., Giordano, F., Glanzman, T., Godfrey, G., Grenier, I.A., Grondin, M.H., Grove, J.E., Guillemot, L., Guiriec, S., Haller, G., Harding, A.K., Hart, P.A., Hays, E., Healey, S.E., Hirayama, M., Hjalmarsdotter, L., Horn, R., Hughes, R.E., Jóhannesson, G., Jóhannesson, G., Johnson, A.S., Johnson, R.P., Johnson, T.J., Johnson, W.N., Kamae, T., Katagiri, H., Kataoka, J., Kavelaars, A., Kawai, N., Kelly, H., Kerr, M., Klamra, W., Knödseder, J., Kocian, M.L., Komin, N., Kuehn, F., Kuss, M., Landriu, D., Latronico, L., Lee, B., Lee, S.H., Lemoine-Goumard, M., Lionetto, A.M., Longo, F., Loparco, F., Lott, B., Lovellette, M.N., Lubrano, P., Madejski, G.M., Makeev, A., Marangelli, B., Massai, M.M., Mazziotta, M.N., McEnery, J.E., Menon, N., Meurer, C., Michelson, P.F., Minuti, M., Mirizzi, N., Mitthumsiri, W., Mizuno, T., Moiseev, A.A., Monte, C., Monzani, M.E., Moretti, E., Morselli, A., Moskalenko, I.V., Murgia, S., Nakamori, T., Nishino, S., Nolan, P.L., Norris, J.P., Nuss, E., Ohno, M., Ohsugi, T., Omodei, N., Orlando, E., Ormes, J.F., Paccagnella, A., Paneque, D., Panetta, J.H., Parent, D., Pearce, M., Pepe, M., Perazzo, A., Pesce-Rollins, M., Picozza, P., Pieri, L., Pinchera, M., Piron, F., Porter, T.A., Poupard, L., Rainò, S., Rando, R., Rapposelli, E., Razzano, M., Reimer, A., Reimer, O., Reposeur, T., Reyes, L.C., Ritz, S., Rochester, L.S., Rodriguez, A.Y., Romani, R.W., Roth, M., Russell, J.J., Ryde, F., Sabatini, S., Sadrozinski, H.F.W., Sanchez, D., Sander, A., Sapozhnikov, L., Parkinson, P.M.S., Scargle, J.D., Schalk, T.L., Scolieri, G., Sgrò, C., Share, G.H., Shaw, M., Shimokawabe, T., Shrader, C., Sierpowska-Bartosik, A., Siskind, E.J., Smith, D.A., Smith, P.D., Spandre, G., Spinelli, P., Starck, J.L., Stephens, T.E., Strickman, M.S., Strong, A.W., Suson, D.J., Tajima, H., Takahashi, H., Takahashi, T., Tanaka, T., Tenze, A., Tether, S., Thayer, J.B., Thayer, J.G., Thompson, D.J., Tibaldo, L., Tibolla, O., Torres, D.F., Tosti, G., Tramacere, A., Turri, M., Usher, T.L., Vilchez, N., Vitale, V., Wang, P., Watters, K., Winer, B.L., Wood, K.S., Ylinen, T., Ziegler, M., 2009. The Large Area Telescope on the Fermi Gamma-Ray Space Telescope Mission. *ApJ* 697, 1071–1102. doi:10.1088/0004-637X/697/2/1071, arXiv:0902.1089.
- Auchère, F., Froment, C., Bocchialini, K., Buchlin, E., Solomon, J., 2016. On the Fourier and Wavelet Analysis of Coronal Time Series. *ApJ* 825, 110. doi:10.3847/0004-637X/825/2/110, arXiv:1606.05251.
- Baghmanyan, V., Gasparyan, S., Sahakyan, N., 2017. Rapid Gamma-Ray

- Variability of NGC 1275. *ApJ* 848, 111. doi:10.3847/1538-4357/aa8c7b, arXiv:1709.03755.
- Begelman, M.C., Blandford, R.D., Rees, M.J., 1980. Massive black hole binaries in active galactic nuclei. *Nature* 287, 307–309. doi:10.1038/287307a0.
- Bégué, D., Sahakyan, N., Dereli-Bégué, H., Giommi, P., Gasparyan, S., Khachatryan, M., Casotto, A., Pe'er, A., 2024. Modeling Blazar Broadband Emission with a Convolutional Neural Network. I. Synchrotron Self-Compton Model. *ApJ* 963, 71. doi:10.3847/1538-4357/ad19cf, arXiv:2311.02979.
- Bellm, E.C., Kulkarni, S.R., Graham, M.J., Dekany, R., Smith, R.M., Riddle, R., Masci, F.J., Helou, G., Prince, T.A., Adams, S.M., Barbarino, C., Barlow, T., Bauer, J., Beck, R., Belicki, J., Biswas, R., Blagorodnova, N., Bodewits, D., Bolin, B., Brinell, V., Brooke, T., Bue, B., Bulla, M., Burruss, R., Cenko, S.B., Chang, C.K., Connolly, A., Coughlin, M., Cromer, J., Cunningham, V., De, K., Delacroix, A., Desai, V., Duev, D.A., Eadie, G., Farnham, T.L., Feeney, M., Feindt, U., Flynn, D., Franckowiak, A., Frederick, S., Fremling, C., Gal-Yam, A., Gezari, S., Giomi, M., Goldstein, D.A., Golkhou, V.Z., Goobar, A., Groom, S., Hacıopians, E., Hale, D., Henning, J., Ho, A.Y.Q., Hover, D., Howell, J., Hung, T., Huppenkothen, D., Imel, D., Ip, W.H., Ivezić, Ž., Jackson, E., Jones, L., Juric, M., Kasliwal, M.M., Kaspi, S., Kaye, S., Kelley, M.S.P., Kowalski, M., Kramer, E., Kupfer, T., Landry, W., Laher, R.R., Lee, C.D., Lin, H.W., Lin, Z.Y., Lunnan, R., Giomi, M., Mahabal, A., Mao, P., Miller, A.A., Monkewitz, S., Murphy, P., Ngeow, C.C., Nordin, J., Nugent, P., Ofek, E., Patterson, M.T., Penprase, B., Porter, M., Rauch, L., Rebbapragada, U., Reiley, D., Rigault, M., Rodriguez, H., van Roestel, J., Rusholme, B., van Santen, J., Schulze, S., Shupe, D.L., Singer, L.P., Soumagnac, M.T., Stein, R., Surace, J., Sollerman, J., Szkody, P., Taddia, F., Terek, S., Van Sistine, A., van Velzen, S., Vestrand, W.T., Walters, R., Ward, C., Ye, Q.Z., Yu, P.C., Yan, L., Zolkower, J., 2019. The Zwicky Transient Facility: System Overview, Performance, and First Results. *PASP* 131, 018002. doi:10.1088/1538-3873/aacbbe, arXiv:1902.01932.
- Blandford, R., Meier, D., Readhead, A., 2019. Relativistic Jets from Active Galactic Nuclei. *ARA&A* 57, 467–509. doi:10.1146/annurev-astro-081817-051948, arXiv:1812.06025.
- Błażejowski, M., Sikora, M., Moderski, R., Madejski, G.M., 2000. Comptonization of Infrared Radiation from Hot Dust by Relativistic Jets in Quasars. *ApJ* 545, 107–116. doi:10.1086/317791, arXiv:astro-ph/0008154.
- Britto, R.J., Bottacini, E., Lott, B., Razaque, S., Buson, S., 2016. Fermi-LAT Observations of the 2014 May–July Outburst from 3C 454.3. *ApJ* 830, 162. doi:10.3847/0004-637X/830/2/162, arXiv:1511.02280.
- Britzen, S., Zajaček, M., Gopal-Krishna, Fendt, C., Kun, E., Jaron, F., Sillanpää, A., Eckart, A., 2023. Precession-induced Variability in AGN Jets and OJ 287. *ApJ* 951, 106. doi:10.3847/1538-4357/acbbcc, arXiv:2307.05838.
- Burrows, D.N., Hill, J.E., Nousek, J.A., Kennea, J.A., Wells, A., Osborne, J.P., Abbey, A.F., Beardmore, A., Mukerjee, K., Short, A.D.T., Chincarini, G., Campana, S., Citterio, O., Moretti, A., Pagani, C., Tagliaferri, G., Giommi, P., Capalbi, M., Tamburelli, F., Angelini, L., Cusumano, G., Bräuninger, H.W., Burkert, W., Hartner, G.D., 2005. The Swift X-Ray Telescope. *Space Sci. Rev.* 120, 165–195. doi:10.1007/s11214-005-5097-2, arXiv:astro-ph/0508071.
- Caproni, A., Abraham, Z., 2004. Can long-term periodic variability and jet helicity in 3C 120 be explained by jet precession? *MNRAS* 349, 1218–1226. doi:10.1111/j.1365-2966.2004.07550.x, arXiv:astro-ph/0312407.
- Caproni, A., Mosquera Cuesta, H.J., Abraham, Z., 2004. Observational Evidence of Spin-induced Precession in Active Galactic Nuclei. *ApJ* 616, L99–L102. doi:10.1086/426863, arXiv:astro-ph/0410450.
- Cash, W., 1979. Parameter estimation in astronomy through application of the likelihood ratio. *ApJ* 228, 939–947. doi:10.1086/156922.
- Cerruti, M., 2020. Leptonic and Hadronic Radiative Processes in Supermassive-Black-Hole Jets. *Galaxies* 8, 72. doi:10.3390/galaxies8040072, arXiv:2012.13302.
- Chambers, K.C., Magnier, E.A., Metcalfe, N., Flewelling, H.A., Huber, M.E., Waters, C.Z., Denneau, L., Draper, P.W., Farrow, D., Finkbeiner, D.P., Holmberg, C., Koppenhoefer, J., Price, P.A., Rest, A., Saglia, R.P., Schlafly, E.F., Smartt, S.J., Sweeney, W., Wainscoat, R.J., Burgett, W.S., Chastel, S., Grav, T., Heasley, J.N., Hodapp, K.W., Jedicke, R., Kaiser, N., Kudritzki, R.P., Luppino, G.A., Lupton, R.H., Monet, D.G., Morgan, J.S., Onaka, P.M., Shiao, B., Stubbs, C.W., Tonry, J.L., White, R., Bañados, E., Bell, E.F., Bender, R., Bernard, E.J., Boegner, M., Boffi, F., Botticella, M.T., Calamida, A., Casertano, S., Chen, W.P., Chen, X., Cole, S., Deacon, N., Frenk, C., Fitzsimmons, A., Gezari, S., Gibbs, V., Goessl, C., Goggia, T., Gourgue, R., Goldman, B., Grant, P., Grebel, E.K., Hambly, N.C., Hasinger, G., Heavens, A.F., Heckman, T.M., Henderson, R., Henning, T., Holman, M., Hopp, U., Ip, W.H., Isani, S., Jackson, M., Keyes, C.D., Koekemoer, A.M., Kotak, R., Le, D., Liska, D., Long, K.S., Lucey, J.R., Liu, M., Martin, N.F., Masci, G., McLean, B., Mindel, E., Misra, P., Morganson, E., Murphy, D.N.A., Obaika, A., Narayan, G., Nieto-Santesteban, M.A., Norberg, P., Peacock, J.A., Pier, E.A., Postman, M., Primak, N., Rae, C., Rai, A., Riess, A., Riffeser, A., Rix, H.W., Röser, S., Russel, R., Rutz, L., Schilbach, E., Schultz, A.S.B., Scolnic, D., Strolger, L., Szalay, A., Seitz, S., Small, E., Smith, K.W., Soderblom, D.R., Taylor, P., Thomson, R., Taylor, A.N., Thakar, A.R., Thiel, J., Thilker, D., Unger, D., Urata, Y., Valenti, J., Wagner, J., Walder, T., Walter, F., Watters, S.P., Werner, S., Wood-Vasey, W.M., Wyse, R., 2016. The Pan-STARRS1 Surveys. arXiv e-prints, arXiv:1612.05560doi:10.48550/arXiv.1612.05560, arXiv:1612.05560.
- Connolly, S.D., 2015. A Python Code for the Emmanoulopoulos et al. [arXiv:1305.0304] Light Curve Simulation Algorithm. arXiv e-prints, arXiv:1503.06676arXiv:1503.06676.
- Conway, J.E., Murphy, D.W., 1993. Helical Jets and the Misalignment Distribution for Core-dominated Radio Sources. *ApJ* 411, 89. doi:10.1086/172809.
- Cortina, J., CTAO LST Collaboration, 2023. First detection of VHE gamma-ray emission from FSRQ OP 313 with LST-1. The Astronomer's Telegram 16381, 1.
- Covino, S., Landoni, M., Sandrinelli, A., Treves, A., 2020. Looking at Blazar Light-curve Periodicities with Gaussian Processes. *ApJ* 895, 122. doi:10.3847/1538-4357/ab8bd4, arXiv:2004.10763.
- Dermer, C.D., Schlickeiser, R., 1994. On the Location of the Acceleration and Emission Sites in Gamma-Ray Blazars. *ApJS* 90, 945. doi:10.1086/191929.
- Dermer, C.D., Schlickeiser, R., Mastichiadis, A., 1992. High-energy gamma radiation from extragalactic radio sources. *A&A* 256, L27–L30.
- Domínguez, A., Primack, J.R., Rosario, D.J., Prada, F., Gilmore, R.C., Faber, S.M., Koo, D.C., Somerville, R.S., Pérez-Torres, M.A., Pérez-González, P., Huang, J.S., Davis, M., Guhathakurta, P., Barmby, P., Conselice, C.J., Lozano, M., Newman, J.A., Cooper, M.C., 2011. Extragalactic background light inferred from AEGIS galaxy-SED-type fractions. *MNRAS* 410, 2556–2578. doi:10.1111/j.1365-2966.2010.17631.x, arXiv:1007.1459.
- Emmanoulopoulos, D., McHardy, I.M., Papadakis, I.E., 2013. Generating artificial light curves: revisited and updated. *MNRAS* 433, 907–927. doi:10.1093/mnras/stt764, arXiv:1305.0304.
- Feroz, F., Hobson, M.P., Bridges, M., 2009. MULTINEST: an efficient and robust Bayesian inference tool for cosmology and particle physics. *MNRAS* 398, 1601–1614. doi:10.1111/j.1365-2966.2009.14548.x, arXiv:0809.3437.
- Gasparyan, S., Bégué, D., Sahakyan, N., 2022. Time-dependent leptohadronic modelling of the emission from blazar jets with SOPRANO: the case of TXS 0506 + 056, 3HSP J095507.9 + 355101, and 3C 279. *MNRAS* 509, 2102–2121. doi:10.1093/mnras/stab2688, arXiv:2110.01549.
- Gasparyan, S., Sahakyan, N., Baghmany, V., Zargaryan, D., 2018. On the Multiwavelength Emission from CTA 102. *ApJ* 863, 114. doi:10.3847/1538-4357/aad234, arXiv:1807.02869.
- Gehrels, N., Chincarini, G., Giommi, P., Mason, K.O., Nousek, J.A., Wells, A.A., White, N.E., Barthelmy, S.D., Burrows, D.N., Cominsky, L.R., Hurley, K.C., Marshall, F.E., Mészáros, P., Roming, P.W.A., Angelini, L., Barbier, L.M., Belloni, T., Campana, S., Caraveo, P.A., Chester, M.M., Citterio, O., Cline, T.L., Cropper, M.S., Cummings, J.R., Dean, A.J., Feigelson, E.D., Fenimore, E.E., Frail, D.A., Fruchter,

- A.S., Garmire, G.P., Gendreau, K., Ghisellini, G., Greiner, J., Hill, J.E., Hunsberger, S.D., Krimm, H.A., Kulkarni, S.R., Kumar, P., Lebrun, F., Lloyd-Ronning, N.M., Markwardt, C.B., Mattson, B.J., Mushotzky, R.F., Norris, J.P., Osborne, J., Paczynski, B., Palmer, D.M., Park, H.S., Parsons, A.M., Paul, J., Rees, M.J., Reynolds, C.S., Rhoads, J.E., Sasseen, T.P., Schaefer, B.E., Short, A.T., Smale, A.P., Smith, I.A., Stella, L., Tagliaferri, G., Takahashi, T., Tashiro, M., Townsley, L.K., Tueller, J., Turner, M.J.L., Vietri, M., Voges, W., Ward, M.J., Willingale, R., Zerbi, F.M., Zhang, W.W., 2004. The Swift Gamma-Ray Burst Mission. *ApJ* 611, 1005–1020. doi:10.1086/422091, arXiv:astro-ph/0405233.
- Ghisellini, G., Della Ceca, R., Volonteri, M., Ghirlanda, G., Tavecchio, F., Foschini, L., Tagliaferri, G., Haardt, F., Pareschi, G., Grindlay, J., 2010. Chasing the heaviest black holes of jetted active galactic nuclei. *MNRAS* 405, 387–400. doi:10.1111/j.1365-2966.2010.16449.x, arXiv:0912.0001.
- Ghisellini, G., Tavecchio, F., 2015. Fermi/LAT broad emission line blazars. *MNRAS* 448, 1060–1077. doi:10.1093/mnras/stv055, arXiv:1501.03504.
- Ghosh, S.K., Tandon, S.N., Joseph, P., Devaraj, A., Shelat, D.S., Stalin, C.S., 2021. Performance of the UVIT Level-2 pipeline. *Journal of Astrophysics and Astronomy* 42, 29. doi:10.1007/s12036-020-09686-z, arXiv:2012.13534.
- H. E. S. S. Collaboration, Aharonian, F., Backes, M., Batzofin, R., Becherini, Y., Berge, D., Bernlöhr, K., Bi, B., Böttcher, M., Boisson, C., Bolmont, J., Brun, F., Bruno, B., Burger-Scheidlin, C., Cecchin Momo, D., Celic, J., Cerruti, M., Chen, A., Chernyakova, M., Chibueze, J.O., Chibueze, O., Cornejo, B., Cotter, G., Damascene Mbarubucyeye, J., Davids, I.D., de Assis Scarpin, J., de Bony de Lavergne, M., de Naurois, M., de Oña Wilhelmi, E., Delgado Giler, A.G., Devin, J., Djannati-Ataï, A., Dmytriiev, A., Egberts, K., Egg, K., Ernenwein, J.P., Esca nuela Nieves, C., Feijen, K., Filipovic, M.D., Fontaine, G., Funk, S., Gabici, S., Genaro, M., Glicenstein, J.F., Glombitza, J., Goswami, P., Heckmann, L., Hess, B., Hinton, J.A., Hofmann, W., Holch, T.L., Holler, M., Horns, D., Jamroz, M., Jankowsky, F., Jaroschewski, I., Jung-Richardt, I., Kasprzak, K., Katarzyński, K., Kerszberg, D., Khélifi, B., Komin, N., Kosack, K., Kostunin, D., Lang, R.G., Lazarević, S., Lemièrre, A., Lenain, J.P., Liniewicz, P., Luashvili, A., Mackey, J., Malyshev, D., Marandon, V., Mayer, M., Mehta, A., Mitchell, A.M.W., Moderski, R., Mohrmann, L., Montanari, A., Moulin, E., Niemiec, J., Moghadam, M.O., Panny, S., Parsons, R.D., Pensec, U., Pichard, P., Preis, T., Pühlhofer, G., Punch, M., Quirrenbach, A., Reimer, A., Reimer, O., Reis, I., Rudak, B., Sabri, K., Sahakian, V., Jimeno, D., Santangelo, A., Sasaki, M., Schüssler, F., Shapopi, J.N.S., Si Said, W., Stawarz, Ł., Steinmassl, S., Takahashi, T., Tanaka, T., Taylor, A.M., Taylor, G.L., Terrier, R., Unbehauen, T., van Eldik, C., Vecchi, M., Venter, C., Vink, J., Wach, T., Wagner, S.J., Wierzcholska, A., Zacharias, M., Zech, A., Zhong, W., 2026. H.E.S.S. detection and multi-wavelength study of the $z \sim 1$ blazar PKS 0346–27. *A&A* 706, A246. doi:10.1051/0004-6361/202557228, arXiv:2512.24228.
- Harrison, F.A., Craig, W.W., Christensen, F.E., Hailey, C.J., Zhang, W.W., Boggs, S.E., Stern, D., Cook, W.R., Forster, K., Giommi, P., Grefenstette, B.W., Kim, Y., Kitaguchi, T., Koglin, J.E., Madsen, K.K., Mao, P.H., Miyasaka, H., Mori, K., Perri, M., Pivovarov, M.J., Puccetti, S., Rana, V.R., Westergaard, N.J., Willis, J., Zoglauer, A., An, H., Bachetti, M., Barrière, N.M., Bellm, E.C., Bhalariao, V., Brejnholt, N.F., Fuerst, F., Liebe, C.C., Markwardt, C.B., Nynka, M., Vogel, J.K., Walton, D.J., Wik, D.R., Alexander, D.M., Cominsky, L.R., Hornschemeier, A.E., Hornstrup, A., Kaspi, V.M., Madejski, G.M., Matt, G., Molendi, S., Smith, D.M., Tomsick, J.A., Ajello, M., Ballantyne, D.R., Baloković, M., Barret, D., Bauer, F.E., Blandford, R.D., Brandt, W.N., Brenneman, L.W., Chiang, J., Chakrabarty, D., Chenevez, J., Comastri, A., Dufour, F., Elvis, M., Fabian, A.C., Farrah, D., Fryer, C.L., Gotthelf, E.V., Grindlay, J.E., Helfand, D.J., Krivonos, R., Meier, D.L., Miller, J.M., Natalucci, L., Ogle, P., Ofek, E.O., Ptak, A., Reynolds, S.P., Rigby, J.R., Tagliaferri, G., Thorsett, S.E., Treister, E., Urry, C.M., 2013. The Nuclear Spectroscopic Telescope Array (NuSTAR) High-energy X-Ray Mission. *ApJ* 770, 103. doi:10.1088/0004-637X/770/2/103, arXiv:1301.7307.
- HI4PI Collaboration, Ben Bekhti, N., Flöer, L., Keller, R., Kerp, J., Lenz, D., Winkel, B., Bailin, J., Calabretta, M.R., Dedes, L., Ford, H.A., Gibson, B.K., Haud, U., Janowiecki, S., Kalberla, P.M.W., Lockman, F.J., McClure-Griffiths, N.M., Murphy, T., Nakanishi, H., Pisano, D.J., Staveley-Smith, L., 2016. HI4PI: A full-sky H I survey based on EBHIS and GASS. *A&A* 594, A116. doi:10.1051/0004-6361/201629178, arXiv:1610.06175.
- Karpov, S., 2025. STDweb: simple transient detection pipeline for the web. *Acta Polytechnica* 65, 50–64. doi:10.14311/AP.2025.65.0050, arXiv:2411.16470.
- Kochanek, C.S., Shappee, B.J., Stanek, K.Z., Holoien, T.W.S., Thompson, T.A., Prieto, J.L., Dong, S., Shields, J.V., Will, D., Britt, C., Perzanowski, D., Pojmański, G., 2017. The All-Sky Automated Survey for Supernovae (ASAS-SN) Light Curve Server v1.0. *PASP* 129, 104502. doi:10.1088/1538-3873/aa80d9, arXiv:1706.07060.
- Kun, E., Jaroschewski, I., Ghorbanietamad, A., Frey, S., Becker Tjus, J., Britzen, S., Gabányi, K.É., Kiselev, V., Schlegel, L., Schroller, M., Reichherzer, P., Cui, L., Wang, X., Shen, Y., 2022. Multimessenger Picture of J1048+7143. *ApJ* 940, 163. doi:10.3847/1538-4357/ac9cce, arXiv:2209.05107.
- Kun, E., Jaroschewski, I., Tjus, J.B., Britzen, S., Frey, S., Gabányi, K.É., Cui, L., Wang, X., Shen, Y., 2024. Follow-up on the Supermassive Black Hole Binary Candidate J1048+7143: Successful Prediction of the Next Gamma-Ray Flare and Refined Binary Parameters in the Framework of the Jet Precession Model. *ApJ* 963, L16. doi:10.3847/2041-8213/ad2767, arXiv:2311.03924.
- Lang, D., Hogg, D.W., Mierle, K., Blanton, M., Roweis, S., 2010. Astrometry.net: Blind Astrometric Calibration of Arbitrary Astronomical Images. *AJ* 139, 1782–1800. doi:10.1088/0004-6256/139/5/1782, arXiv:0910.2233.
- Larwood, J., 1998. On the precession of accretion discs in X-ray binaries. *MNRAS* 299, L32–L36. doi:10.1046/j.1365-8711.1998.01978.x, arXiv:astro-ph/9806348.
- Liska, M., Hesp, C., Tchekhovskoy, A., Ingram, A., van der Klis, M., Markoff, S., 2018. Formation of precessing jets by tilted black hole discs in 3D general relativistic MHD simulations. *MNRAS* 474, L81–L85. doi:10.1093/mnras/1/slx174, arXiv:1707.06619.
- Lister, M.L., Cohen, M.H., Homan, D.C., Kadler, M., Kellermann, K.I., Kovalev, Y.Y., Ros, E., Savolainen, T., Zensus, J.A., 2009. MOJAVE: Monitoring of Jets in Active Galactic Nuclei with VLBA Experiments. VI. Kinematics Analysis of a Complete Sample of Blazar Jets. *AJ* 138, 1874–1892. doi:10.1088/0004-6256/138/6/1874, arXiv:0909.5100.
- Lott, B., Escande, L., Larsson, S., Ballet, J., 2012. An adaptive-binning method for generating constant-uncertainty/constant-significance light curves with Fermi-LAT data. *A&A* 544, A6. doi:10.1051/0004-6361/201218873, arXiv:1201.4851.
- Mainzer, A., Bauer, J., Grav, T., Masiero, J., Cutri, R.M., Dailey, J., Eisenhardt, P., McMillan, R.S., Wright, E., Walker, R., Jedicke, R., Spahr, T., Tholen, D., Alles, R., Beck, R., Brandenburg, H., Conrow, T., Evans, T., Fowler, J., Jarrett, T., Marsh, K., Masci, F., McCallon, H., Wheelock, S., Wittman, M., Wyatt, P., DeBaun, E., Elliott, G., Elsbury, D., Gautier, IV, T., Gomillion, S., Leisawitz, D., Maleszewski, C., Micheli, M., Wilkins, A., 2011. Preliminary Results from NEOWISE: An Enhancement to the Wide-field Infrared Survey Explorer for Solar System Science. *ApJ* 731, 53. doi:10.1088/0004-637X/731/1/53, arXiv:1102.1996.
- Mattox, J.R., Bertsch, D.L., Chiang, J., Dingus, B.L., Digel, S.W., Esposito, J.A., Fierro, J.M., Hartman, R.C., Hunter, S.D., Kanbach, G., Kniffen, D.A., Lin, Y.C., Macomb, D.J., Mayer-Hasselwander, H.A., Michelson, P.F., von Montigny, C., Mukherjee, R., Nolan, P.L., Ramanamurthy, P.V., Schneid, E., Sreekumar, P., Thompson, D.J., Willis, T.D., 1996. The Likelihood Analysis of EGRET Data. *ApJ* 461, 396. doi:10.1086/177068.
- Middei, R., Giommi, P., Perri, M., Turriziani, S., Sahakyan, N., Chang, Y.L., Leto, C., Verrecchia, F., 2022. The first hard X-ray spectral catalogue of Blazars observed by NuSTAR. *MNRAS* 514, 3179–3190. doi:10.1093/mnras/stac1185, arXiv:2205.05089.
- Ostorero, L., Villata, M., Raiteri, C.M., 2004. Helical jets in blazars. Interpretation of the multifrequency long-term variability of <ASTROBJ>AO 0235+16</ASTROBJ>. *A&A* 419, 913–925. doi:10.1051/0004-6361:20035813, arXiv:astro-ph/0402551.
- Paliya, V.S., Domínguez, A., Ajello, M., Olmo-García, A., Hartmann, D.,

2021. The Central Engines of Fermi Blazars. *ApJS* 253, 46. doi:10.3847/1538-4365/abe135, arXiv:2101.10849.
- Peñil, P., Ajello, M., Buson, S., Domínguez, A., Westernacher-Schneider, J.R., Rico, A., Adhikari, S., Zrake, J., 2025. Search for periodic variability in γ -ray blazars Using Fermi-LAT. *MNRAS* 541, 2955–2977. doi:10.1093/mnras/staf1108, arXiv:2211.01894.
- Peñil, P., Domínguez, A., Buson, S., Ajello, M., Otero-Santos, J., Barrio, J.A., Nemmen, R., Cutini, S., Rani, B., Franckowiak, A., Cavazzuti, E., 2020. Systematic Search for γ -Ray Periodicity in Active Galactic Nuclei Detected by the Fermi Large Area Telescope. *ApJ* 896, 134. doi:10.3847/1538-4357/ab910d, arXiv:2002.00805.
- Pillitteri, I., Colombo, S., Micela, G., Wolk, S.J., 2023. The X-ray activity of F stars with hot Jupiters: KELT-24 versus WASP-18. *A&A* 673, A61. doi:10.1051/0004-6361/202245467, arXiv:2304.00854.
- Raiteri, C.M., Villata, M., Acosta-Pulido, J.A., Agudo, I., Arkharov, A.A., Bachev, R., Baida, G.V., Benítez, E., Borman, G.A., Boschin, W., Bozhilov, V., Butuzova, M.S., Calcidese, P., Carnerero, M.I., Carosati, D., Casadio, C., Castro-Segura, N., Chen, W.P., Damljanovic, G., D’Ammando, F., di Paola, A., Echevarría, J., Efimova, N.V., Ehgamberdiev, S.A., Espinosa, C., Fuentes, A., Giunta, A., Gómez, J.L., Grishina, T.S., Gurwell, M.A., Hiriart, D., Jermak, H., Jordan, B., Jorstad, S.G., Joshi, M., Kopatskaya, E.N., Kuratov, K., Kurtanidze, O.M., Kurtanidze, S.O., Lähteenmäki, A., Larionov, V.M., Larionova, E.G., Larionova, L.V., Lázaro, C., Lin, C.S., Malmrose, M.P., Marscher, A.P., Matsumoto, K., McBreen, B., Michel, R., Mihov, B., Minev, M., Mirzaqulov, D.O., Mokrushina, A.A., Molina, S.N., Moody, J.W., Morozova, D.A., Nazarov, S.V., Nikolashvili, M.G., Ohlert, J.M., Okhmat, D.N., Ovcharov, E., Pinna, F., Polakis, T.A., Protasio, C., Pursimo, T., Redondo-Lorenzo, F.J., Rizzi, N., Rodríguez-Coira, G., Sadakane, K., Sadun, A.C., Samal, M.R., Savchenko, S.S., Semkov, E., Skiff, B.A., Slavcheva-Mihova, L., Smith, P.S., Steele, I.A., Strigachev, A., Tammi, J., Thum, C., Tornikoski, M., Troitskaya, Y.V., Troitsky, I.S., Vasilyev, A.A., Vince, O., 2017. Blazar spectral variability as explained by a twisted inhomogeneous jet. *Nature* 552, 374–377. doi:10.1038/nature24623, arXiv:1712.02098.
- Rani, B., Lott, B., Krichbaum, T.P., Fuhrmann, L., Zensus, J.A., 2013. Constraining the location of rapid gamma-ray flares in the flat spectrum radio quasar 3C 273. *A&A* 557, A71. doi:10.1051/0004-6361/201321440, arXiv:1307.0854.
- Ren, H.X., Cerruti, M., Sahakyan, N., 2023. Quasi-periodic oscillations in the γ -ray light curves of bright active galactic nuclei. *A&A* 672, A86. doi:10.1051/0004-6361/202244754, arXiv:2204.13051.
- Rieger, F.M., 2004. On the Geometrical Origin of Periodicity in Blazar-type Sources. *ApJ* 615, L5–L8. doi:10.1086/426018, arXiv:astro-ph/0410188.
- Robert, V., Desmars, J., Lainey, V., Arlot, J.E., Perlbarg, A.C., Horville, D., Abouadarham, J., Etienne, C., Guérard, J., Ilovaisky, S., Khovritchev, M.Y., Le Poncin-Lafitte, C., Le Van Suu, A., Neiner, C., Pascu, D., Poirier, L., Schneider, J., Tanga, P., Valls-Gabaud, D., 2021. The NAROO digitization center. Overview and scientific program. *A&A* 652, A3. doi:10.1051/0004-6361/202140472.
- Romero, G.E., Chajet, L., Abraham, Z., Fan, J.H., 2000. Beaming and precession in the inner jet of 3C 273 — II. The central engine. *A&A* 360, 57–64.
- Roming, P.W.A., Kennedy, T.E., Mason, K.O., Nousek, J.A., Ahr, L., Bingham, R.E., Broos, P.S., Carter, M.J., Hancock, B.K., Huckler, H.E., Hunsberger, S.D., Kawakami, H., Killough, R., Koch, T.S., McLelland, M.K., Smith, K., Smith, P.J., Soto, J.C., Boyd, P.T., Breeveld, A.A., Holland, S.T., Ivanushkina, M., Pryzby, M.S., Still, M.D., Stock, J., 2005. The Swift Ultra-Violet/Optical Telescope. *Space Sci. Rev.* 120, 95–142. doi:10.1007/s11214-005-5095-4, arXiv:astro-ph/0507413.
- Sahakyan, N., 2021. Modelling the broad-band emission of 3C 454.3. *MNRAS* 504, 5074–5086. doi:10.1093/mnras/stab1135, arXiv:2104.09831.
- Sahakyan, N., Baghmanyan, V., Zargaryan, D., 2018. Fermi-LAT observation of nonblazar AGNs. *A&A* 614, A6. doi:10.1051/0004-6361/201732304, arXiv:1801.09381.
- Sahakyan, N., Bégué, D., Casotto, A., Dereli-Bégué, H., Giommi, P., Gasparyan, S., Vardanyan, V., Khachatryan, M., Pe’er, A., 2024a. Modeling Blazar Broadband Emission with Convolutional Neural Networks. II. External Compton Model. *ApJ* 971, 70. doi:10.3847/1538-4357/ad5351, arXiv:2402.07495.
- Sahakyan, N., Bégué, D., Casotto, A., Dereli-Bégué, H., Vardanyan, V., Khachatryan, M., Giommi, P., Pe’er, A., 2025. Modeling Blazar Broadband Emission with Convolutional Neural Networks. III. Proton Synchrotron and Hybrid Models. *ApJ* 990, 222. doi:10.3847/1538-4357/adf734, arXiv:2506.23885.
- Sahakyan, N., Gasparyan, S., 2017. High energy gamma-ray emission from PKS 1441+25. *MNRAS* 470, 2861–2869. doi:10.1093/mnras/stx1402, arXiv:1706.01611.
- Sahakyan, N., Giommi, P., 2022. A 13-yr-long broad-band view of BL Lac. *MNRAS* 513, 4645–4656. doi:10.1093/mnras/stac1011, arXiv:2108.12232.
- Sahakyan, N., Israyelyan, D., Harutyunyan, G., Gasparyan, S., Vardanyan, V., Khachatryan, M., 2022. Modelling the time variable spectral energy distribution of the blazar CTA 102 from 2008 to 2022. *MNRAS* 517, 2757–2768. doi:10.1093/mnras/stac2875, arXiv:2210.04663.
- Sahakyan, N., Vardanyan, V., Giommi, P., Bégué, D., Israyelyan, D., Harutyunyan, G., Manvelyan, M., Khachatryan, M., Dereli-Bégué, H., Gasparyan, S., 2024b. Markarian Multiwavelength Data Center (MMDC): A Tool for Retrieving and Modeling Multitemporal, Multiwavelength, and Multimessenger Data from Blazar Observations. *AJ* 168, 289. doi:10.3847/1538-3881/ad8231, arXiv:2410.01207.
- Scargle, J.D., Norris, J.P., Jackson, B., Chiang, J., 2013. Studies in Astronomical Time Series Analysis. VI. Bayesian Block Representations. *ApJ* 764, 167. doi:10.1088/0004-637X/764/2/167, arXiv:1207.5578.
- Shappee, B.J., Prieto, J.L., Grupe, D., Kochanek, C.S., Stanek, K.Z., De Rosa, G., Mathur, S., Zu, Y., Peterson, B.M., Pogge, R.W., Komossa, S., Im, M., Jencson, J., Holoiien, T.W.S., Basu, U., Beacom, J.F., Szczygiel, D.M., Brimacombe, J., Adams, S., Campillay, A., Choi, C., Contreras, C., Dietrich, M., Dubberley, M., Elphick, M., Foale, S., Giustini, M., Gonzalez, C., Hawkins, E., Howell, D.A., Hsiao, E.Y., Koss, M., Leighly, K.M., Morrell, N., Mudd, D., Mullins, D., Nugent, J.M., Parrent, J., Phillips, M.M., Pojmanski, G., Rosing, W., Ross, R., Sand, D., Terndrup, D.M., Valenti, S., Walker, Z., Yoon, Y., 2014. The Man behind the Curtain: X-Rays Drive the UV through NIR Variability in the 2013 Active Galactic Nucleus Outburst in NGC 2617. *ApJ* 788, 48. doi:10.1088/0004-637X/788/1/48, arXiv:1310.2241.
- Sikora, M., Begelman, M.C., Rees, M.J., 1994. Comptonization of Diffuse Ambient Radiation by a Relativistic Jet: The Source of Gamma Rays from Blazars? *ApJ* 421, 153. doi:10.1086/173633.
- Singh, K.P., Stewart, G.C., Westergaard, N.J., Bhattacharayya, S., Chandra, S., Chitnis, V.R., Dewangan, G.C., Kothare, A.T., Mirza, I.M., Mukerjee, K., Navalkar, V., Shah, H., Abbey, A.F., Beardmore, A.P., Kotak, S., Kamble, N., Vishwakarama, S., Pathare, D.P., Risbud, V.M., Koyande, J.P., Stevenson, T., Bicknell, C., Crawford, T., Hansford, G., Peters, G., Sykes, J., Agarwal, P., Sebastian, M., Rajarajan, A., Nagesh, G., Narendra, S., Ramesh, M., Rai, R., Navalgund, K.H., Sarma, K.S., Pandiyan, R., Subbarao, K., Gupta, T., Thakkar, N., Singh, A.K., Bajpai, A., 2017. Soft X-ray Focusing Telescope Aboard AstroSat: Design, Characteristics and Performance. *Journal of Astrophysics and Astronomy* 38, 29. doi:10.1007/s12036-017-9448-7.
- Sobacchi, E., Sormani, M.C., Stamerra, A., 2017. A model for periodic blazars. *MNRAS* 465, 161–172. doi:10.1093/mnras/stw2684, arXiv:1610.04709.
- Stirling, A.M., Cawthorne, T.V., Stevens, J.A., Jorstad, S.G., Marscher, A.P., Lister, M.L., Gómez, J.L., Smith, P.S., Agudo, I., Gabuzda, D.C., Robson, E.I., Gear, W.K., 2003. Discovery of a precessing jet nozzle in BL Lacertae. *MNRAS* 341, 405–422. doi:10.1046/j.1365-8711.2003.06448.x.
- Torrence, C., Compo, G.P., 1998. A Practical Guide to Wavelet Analysis. *Bulletin of the American Meteorological Society* 79, 61–78. URL: [https://doi.org/10.1175/1520-0477\(1998\)079<0061:APGTWA>2.0.CO;2](https://doi.org/10.1175/1520-0477(1998)079<0061:APGTWA>2.0.CO;2), doi:10.1175/1520-0477(1998)079<0061:APGTWA>2.0.CO;2, arXiv:https://journals.ametsoc.org/bams/article-pdf/79/1/61/3730243/1520-0477(1998)079<0061:APGTWA>2.0.CO;2
- Urry, C.M., Padovani, P., 1995. Unified Schemes for Radio-Loud Active Galactic Nuclei. *PASP* 107, 803. doi:10.1086/133630, arXiv:astro-ph/9506063.

- Valtonen, M.J., Nilsson, K., Villforth, C., Lehto, H.J., Takalo, L.O., Lindfors, E., Sillanpää, A., Hentunen, V.P., Mikkola, S., Zola, S., Drozd, M., Koziel, D., Ogloza, W., Kurpinska-Winiarska, M., Siwak, M., Winiarski, M., Heidt, J., Kidger, M., Pursimo, T., Wu, J.H., Zhou, X., Sadakane, K., Marchev, D., Nissinen, M., Niarchos, P., Liakos, A., Gazeas, K., Dogru, S., Poyner, G., Dietrich, M., Assef, R., Atlee, D., Bird, J., DePoy, D., Eastman, J., Peeples, M., Prieto, J., Watson, L., Yee, J., Mattingly, A., Ohlert, J., 2009. Tidally Induced Outbursts in OJ 287 during 2005-2008. *ApJ* 698, 781–785. doi:10.1088/0004-637X/698/1/781.
- Villata, M., Raiteri, C.M., 1999. Helical jets in blazars. I. The case of MKN 501. *A&A* 347, 30–36.
- Wang, G.G., Cai, J.T., Fan, J.H., 2022. A Possible 3 yr Quasi-periodic Oscillation in γ -Ray Emission from the FSRQ S5 1044+71. *ApJ* 929, 130. doi:10.3847/1538-4357/ac5b08, arXiv:2203.02168.
- Wang, J.J., Yi, T.F., Zhang, Y., Lu, H., Shen, Y., Mao, L., Dong, L., 2025. Two Repeated Quasi-periodic Oscillations in the FSRQ S5 1044+71 Observed by TESS. *Research in Astronomy and Astrophysics* 25, 025004. doi:10.1088/1674-4527/ada2e7, arXiv:2501.12556.
- Yang, S., Yan, D., Zhang, P., Dai, B., Zhang, L., 2021. Gaussian Process Modeling Fermi-LAT γ -Ray Blazar Variability: A Sample of Blazars with γ -Ray Quasi-periodicities. *ApJ* 907, 105. doi:10.3847/1538-4357/abcbbf, arXiv:2011.10186.
- Zargaryan, D., Gasparyan, S., Baghmanyan, V., Sahakyan, N., 2017. Comparing 3C 120 jet emission at small and large scales. *A&A* 608, A37. doi:10.1051/0004-6361/201731601, arXiv:1709.05175.
- Zhou, J., Wang, Z., Chen, L., Wiita, P.J., Vadakkumthani, J., Morrell, N., Zhang, P., Zhang, J., 2018. A 34.5 day quasi-periodic oscillation in γ -ray emission from the blazar PKS 2247-131. *Nature Communications* 9, 4599. doi:10.1038/s41467-018-07103-2, arXiv:1811.02738.

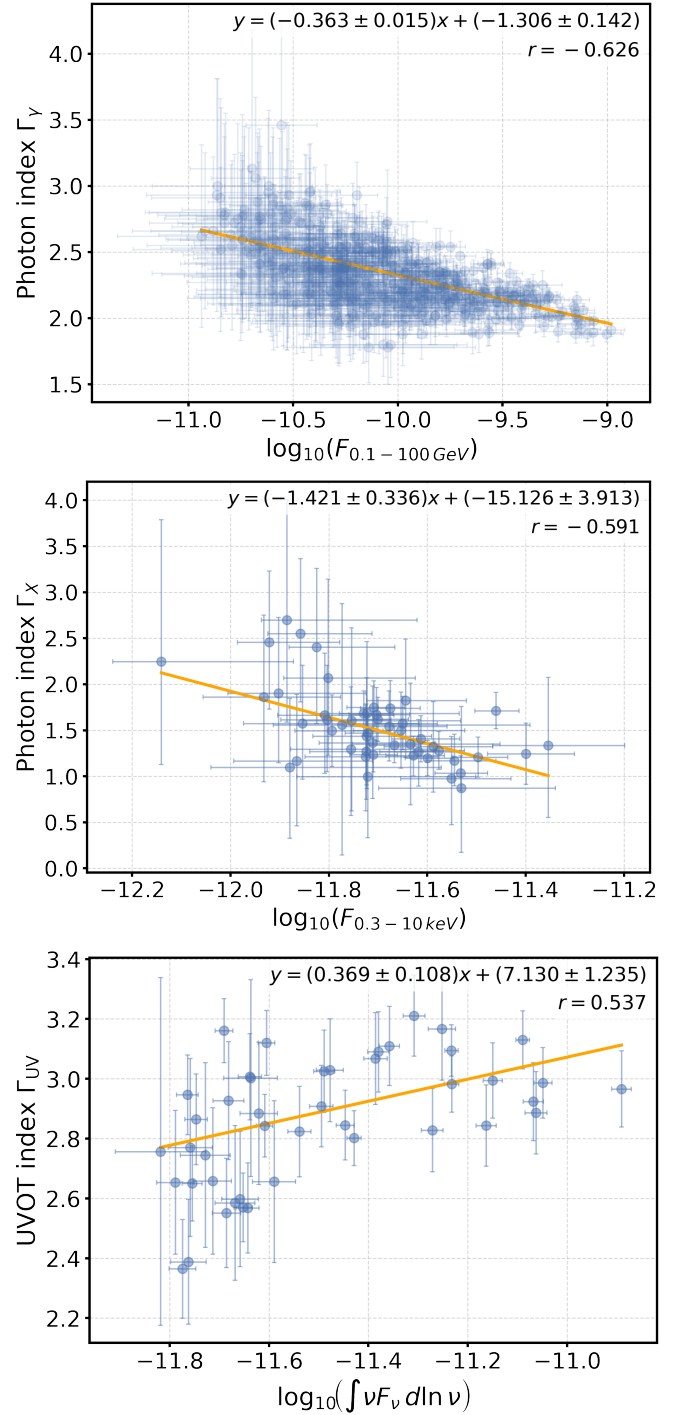


Figure 2: Spectral variability in S5 1044+71. From top to bottom: γ -ray photon index vs the logarithm of the integral photon flux (100 MeV to 100 GeV); X-ray photon index vs the logarithm of the integral photon flux (0.3 keV to 10 keV); optical/UV photon index vs the logarithm of the integral photon flux (from V to W2 UVOT filter).

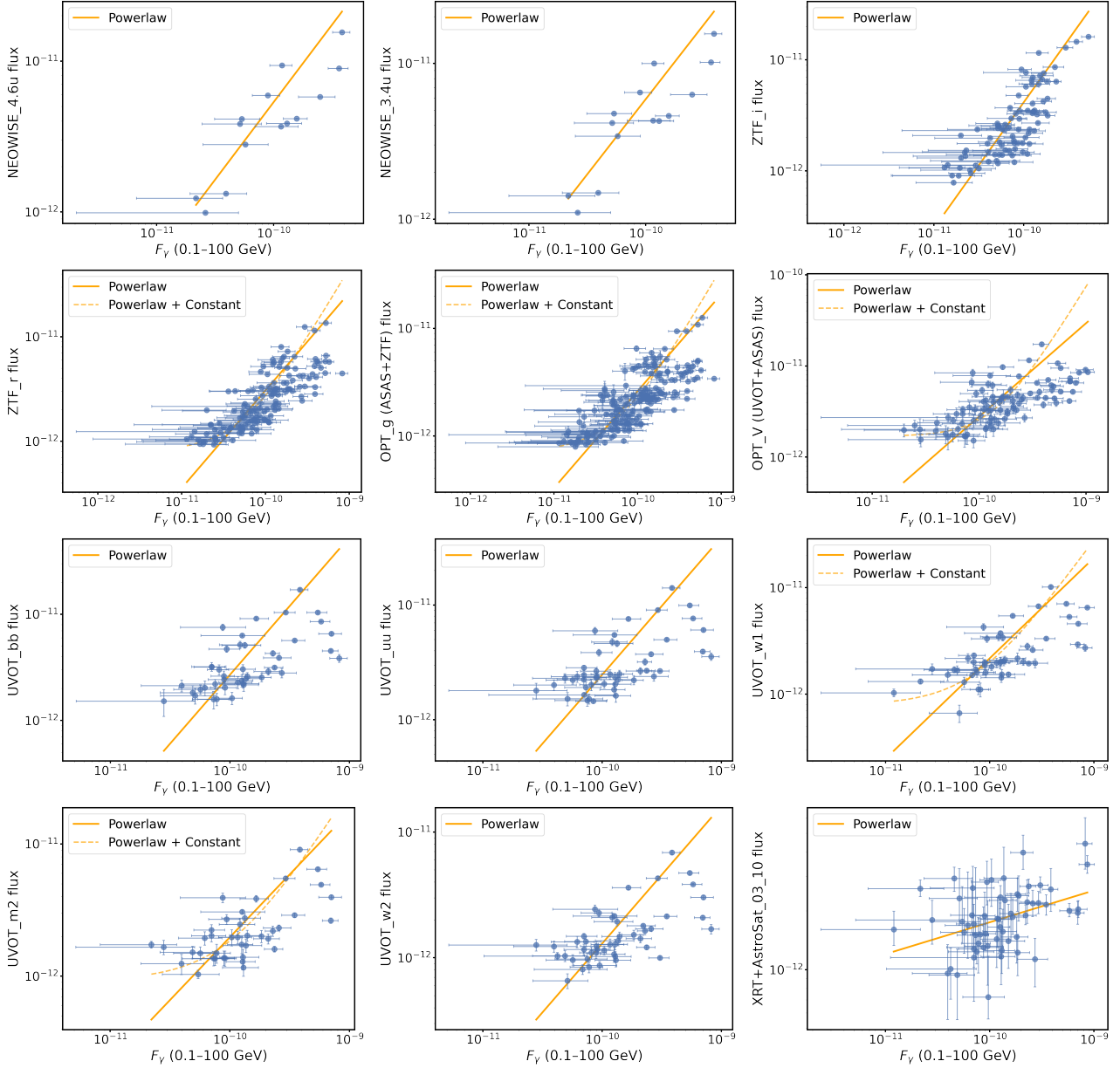


Figure 3: MWL correlation plots with respect to the integral γ -ray photon flux between 100 MeV and 100 GeV. From top to bottom and left to right, the quantities on the y-axis are: NEOWISE flux at $4.6\mu\text{m}$; NEOWISE flux at $3.4\mu\text{m}$; ZTF i filter flux; ZTF r filter flux; ASAS-SN and ZTF g filter flux; ASAS-SN and UVOT V filter flux; UVOT b filter flux; UVOT u filter flux; UVOT w1 filter flux; UVOT M2 filter flux; UVOT W2 filter flux; XRT and *AstroSat*-SXT integral photon flux between 0.3 and 10 keV.

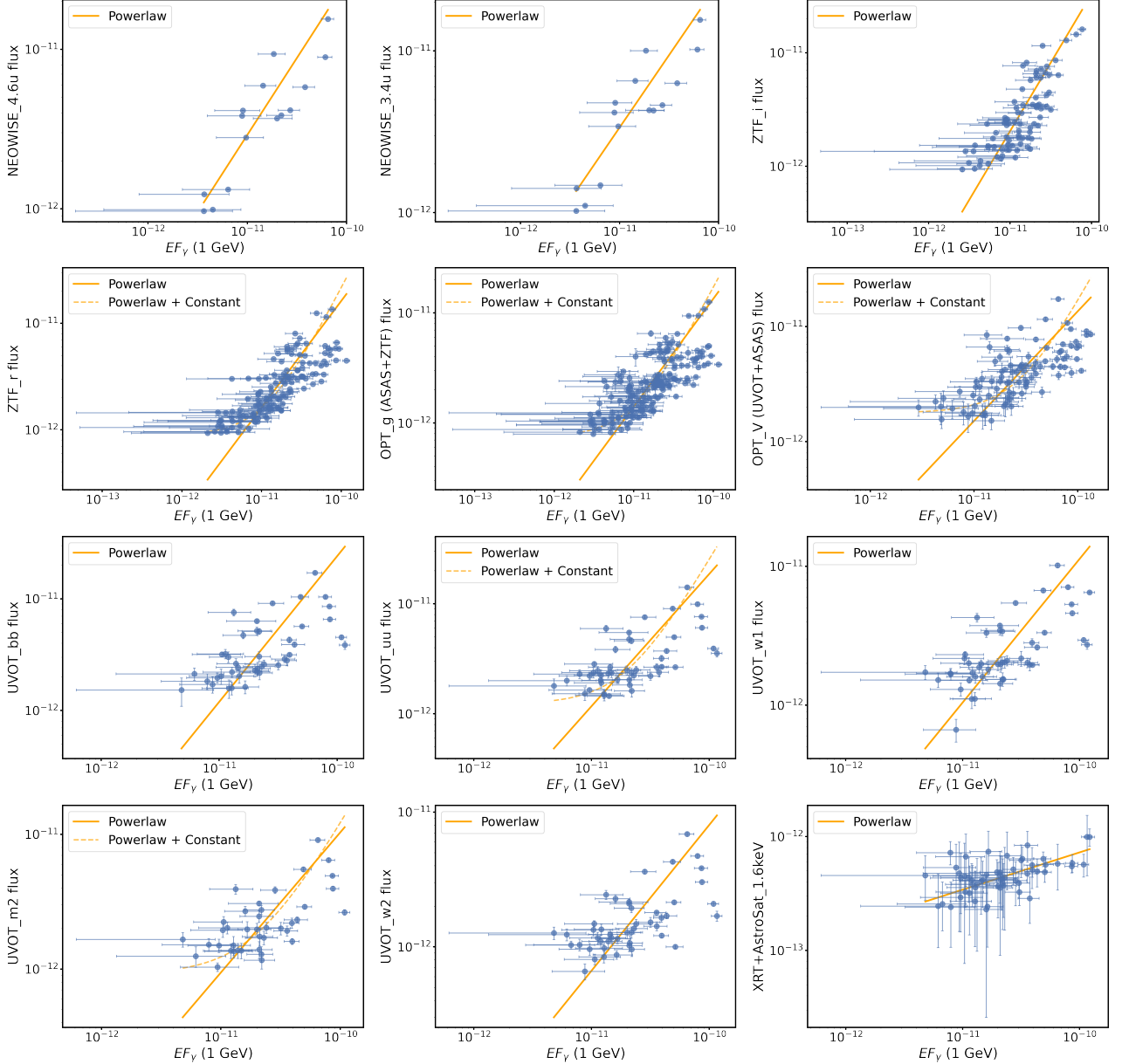


Figure 4: MWL correlation plots with respect to the γ -ray spectral energy distribution evaluated at 1 GeV. From top to bottom and left to right, the quantities on the y-axis are: NEOWISE flux at $4.6\mu\text{m}$; NEOWISE flux at $3.4\mu\text{m}$; ZTF i filter flux; ZTF r filter flux; ASAS-SN and ZTF g filter flux; ASAS-SN and UVOT V filter flux; UVOT b filter flux; UVOT u filter flux; UVOT w1 filter flux; UVOT M2 filter flux; UVOT W2 filter flux; XRT and *AstroSat*-XRT spectral energy distribution evaluated at 1.6 keV.

A precessing jet from a supermassive black hole

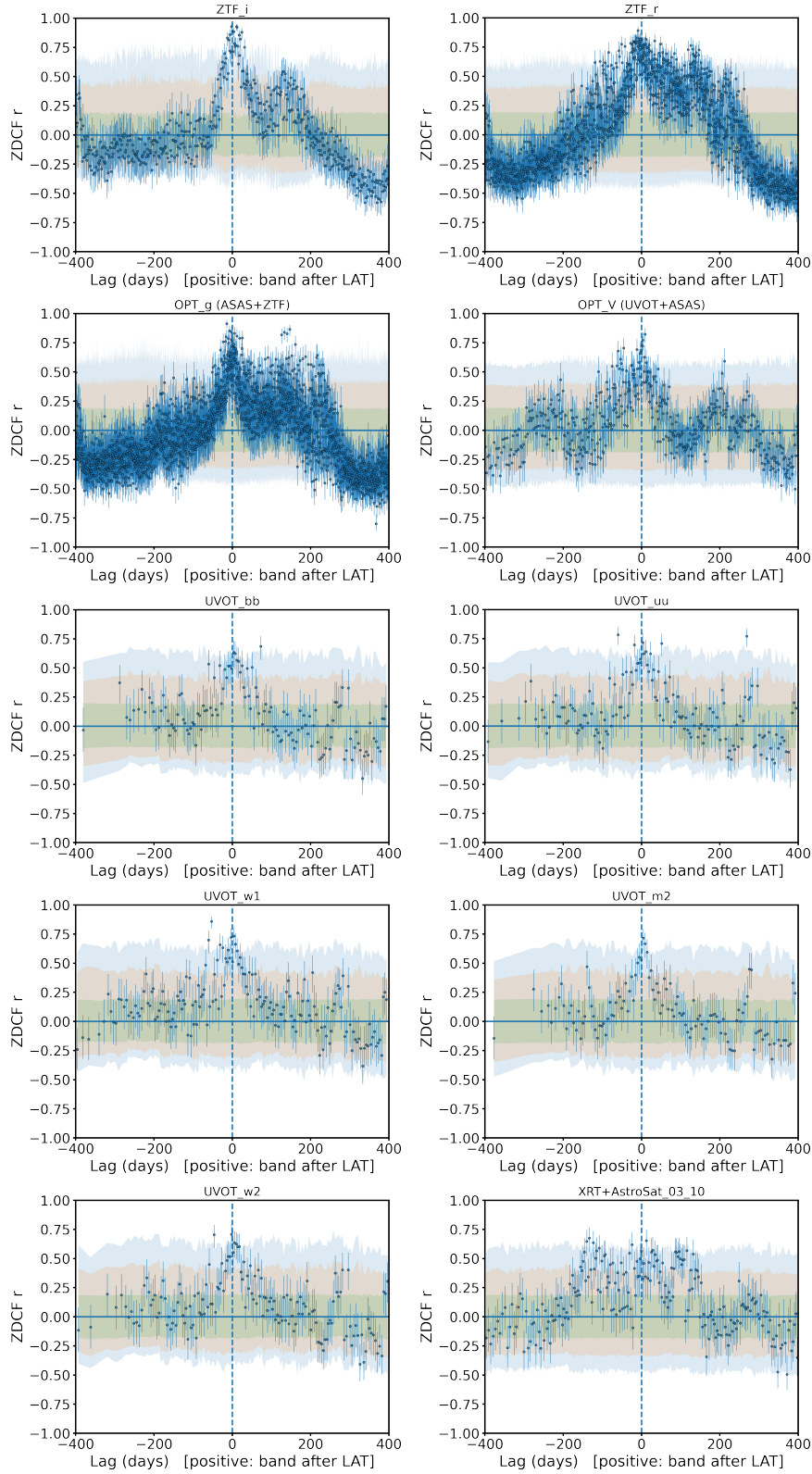


Figure 5: z-transformed discrete correlation function between MWL bands and the γ -ray integral photon flux. From top to bottom and left to right, the MWL band used is: ZTF i filter flux; ZTF r filter flux; ASAS-SN and ZTF g filter flux; ASAS-SN and UVOT V filter flux; UVOT b filter flux; UVOT u filter flux; UVOT w1 filter flux; UVOT M2 filter flux; UVOT W2 filter flux; XRT and *AstroSat*-XRT spectral energy distribution evaluated at 1.6 keV.

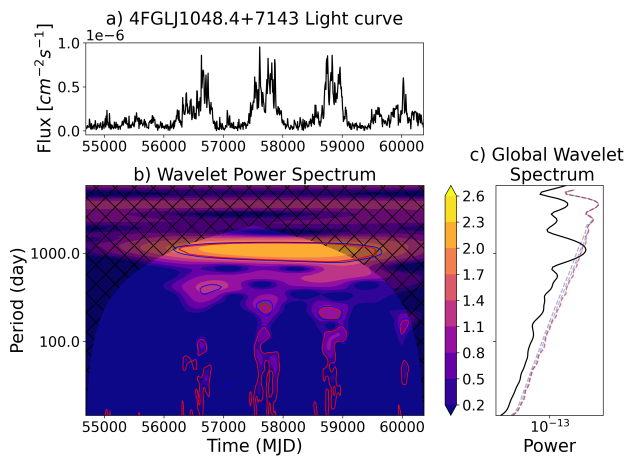


Figure 6: CWT for the monthly binned light curve of S5 1044+71. a) is the *Fermi*-LAT light curve, b) is the wavelet power spectrum and c) the global wavelet spectrum.

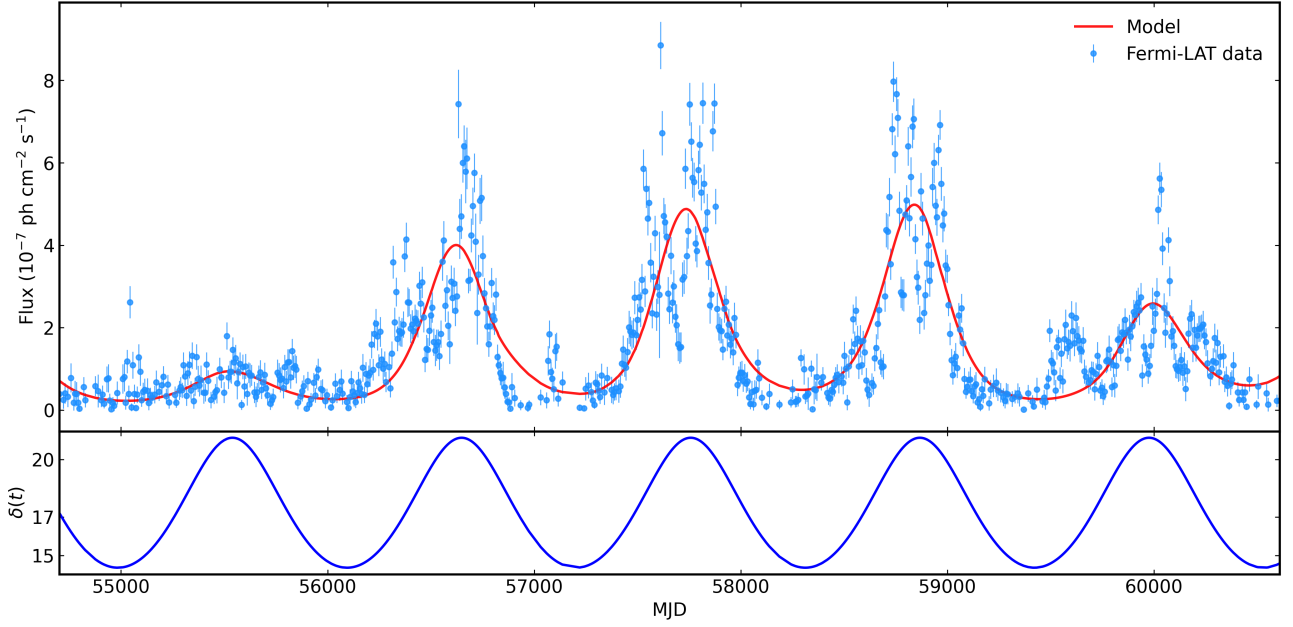


Figure 7: *Top panel:* *Fermi-LAT* γ -ray light curve of S5 1044+71 compared with the best-fit jet-precession model (solid line). The model accounts for long-term quasi-periodic modulation through periodic variations of the Doppler factor, while a low-frequency polynomial baseline captures slower trends not reproduced by pure geometrical effects. *Bottom panel:* Temporal evolution of the Doppler factor $\delta(t)$ inferred from the precession geometry.

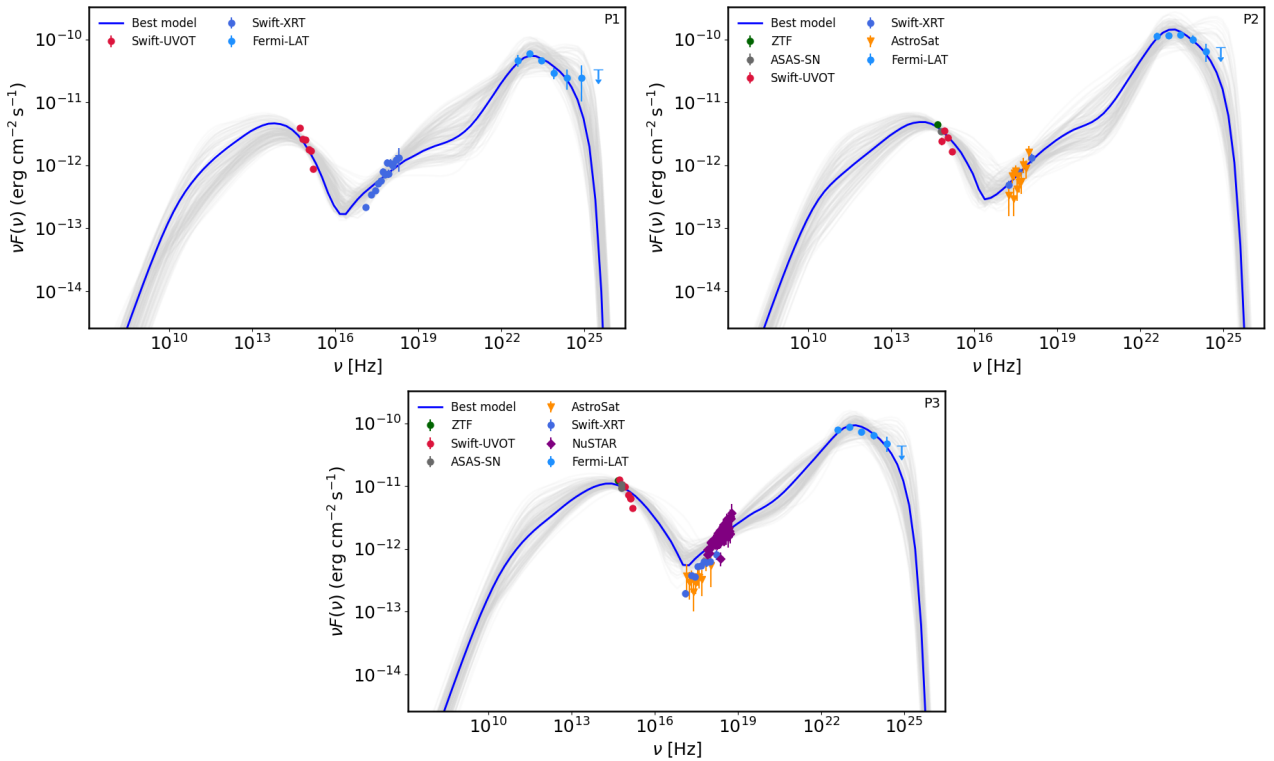


Figure 8: Broadband SEDs of S5 1044+71 during the three activity periods P1–P3. MWL data from ZTF, ASAS-SN, *Swift-UVOT*, *Swift-XRT*, *AstroSat*, *NuSTAR*, and *Fermi-LAT* are shown with different symbols and colors, as indicated in the legends. The blue solid line represents the best-fit leptonic emission model for each period, while the gray curves show the model uncertainty. In all cases, the model include attenuation due to EBL absorption, computed using the model of Domínguez et al. (2011).